## Interplay of Hidden Orbital Order and Superconductivity in CeCoIn<sub>5</sub>

Weijiong Chen<sup>1</sup>§, Clara Neerup Breiø<sup>2</sup>§, Freek Massee§³, M.P. Allan⁴, C. Petrovic⁵, I.C. Séamus Davis¹,6,7,8, P.I. Hirschfeld⁴, Brian M. Andersen² and Andreas Kreisel²,10

- 1. Clarendon Laboratory, University of Oxford, Oxford, OX1 3PU, UK
- 2. Niels Bohr Institute, University of Copenhagen, 2100, Copenhagen, Denmark
- 3. Laboratoire de Physique des Solides (CNRS UMR 8502), Bâtiment 510, Université Paris-Sud/Université Paris-Saclay, 91405 Orsay, France
- 4. Leiden Institute of Physics, Leiden University, P.O. Box 9504, 2300 RA, Leiden, The Netherlands
- 5. CMPMS Department, Brookhaven National Laboratory, Upton, NY 11973, USA.
- 6. LASSP, Department of Physics, Cornell University, Ithaca NY 14850, USA
- 7. Department of Physics, University College Cork, Cork T12 R5C, Ireland
- 8. Max-Planck Institute for Chemical Physics of Solids, D-01187 Dresden, Germany
- 9. Department of Physics, University of Florida, Gainesville, FL 32611, USA.
- 10. Inst. für Theoretische Physik, Universität Leipzig, Brüderstr. 16, Leipzig 04103, Germany
- § These authors contributed equally to this project.

ABSTRACT: Visualizing atomic-orbital degrees of freedom is a frontier challenge in scanned microscopy. Some types of orbital order are virtually imperceptible to normal scattering techniques because they do not reduce the overall crystal lattice symmetry. A good example is  $d_{xz}/d_{yz}$  ( $\pi$ , $\pi$ ) orbital order in tetragonal lattices. For enhanced detectability, here we consider the quasiparticle scattering interference (QPI) signature of such ( $\pi$ , $\pi$ ) orbital order in both normal and superconducting phases. The theory reveals that sublattice-specific QPI signatures generated by the orbital order should emerge strongly in the superconducting phase. Sublattice-resolved QPI visualization in superconducting CeCoIn<sub>5</sub> then reveals two orthogonal QPI patterns at lattice-substitutional impurity atoms. We analyze the energy dependence of these two orthogonal QPI patterns and find the intensity peaked near E=0, as predicted when such ( $\pi$ , $\pi$ ) orbital order is intertwined with d-wave superconductivity. Sublattice-resolved superconductive QPI techniques thus represent a new approach for study of hidden orbital order.

#### **Introduction:**

In a crystalline metal, strong electronic correlations occurring between electrons derived from different orbitals in the same atom can yield an orbital-selective Hund's metal state<sup>1,2</sup>, or even orbital-selective superconductivity<sup>3,4,5</sup>. Similarly, symmetry breaking orbital order may occur, with one of the most famous cases being in the Fe-based high temperature superconductors<sup>6,7</sup>. However, some types of orbital order are almost indiscernible because they do not occur with any lattice distortion which reduces the overall crystal lattice symmetry. For example,  $(\pi,\pi)$  orbital order in a tetragonal array of transition-metal atoms occurs when the degeneracy of  $d_{xz}$  and  $d_{yz}$  orbitals is lifted and each predominates energetically over the other at alternating lattice sites (Fig. 1a). This subtle state does not alter the crystal lattice symmetry meaning that it is virtually invisible to normal photon and neutron scattering techniques, since these techniques are mainly sensitive to the core electron scattering and the nuclear scattering, respectively<sup>8,9</sup>. By contrast, conventional scanning tunneling microscopy (STM) has reported evidence for  $(\pi,\pi)$  orbital order on the surface of CeCoIn5<sup>10</sup>, revealing an opportunity for quasiparticle scattering interference (QPI) imaging , a powerful technique for detecting subtle orbital selective effects<sup>3,11</sup>.

The QPI effect<sup>12,13</sup> occurs when an impurity atom/vacancy scatters quasiparticles which then interfere to produce characteristic modulations of the density-of-states  $\delta N$  (r, E) surrounding each impurity site. Impurity scattering is usually studied by using  $|\delta N(q, E)|$ , the square root of the power-spectral-density Fourier transform of the perturbation to the density of states by the impurity

$$\delta N(\mathbf{q}, E) = -\frac{1}{\pi} \text{Tr} \left( \text{Im} \sum_{\mathbf{k}} \left( G(\mathbf{k}, E + i\eta) T(E) G(\mathbf{k} + \mathbf{q}, E + i\eta) \right) \right)$$
(1)

Here  $G(\mathbf{k}, E + i\eta)$  is the electron propagator  $G(\mathbf{k}, E + i\eta) = 1/(E + i\eta - E_0(\mathbf{k}) - \Sigma(\mathbf{k}, E + i\eta))$  of a quasiparticle state  $|\mathbf{k}\rangle$  with momentum  $\mathbf{k}$ , and  $\Sigma(\mathbf{k}, E + i\eta) = \text{Re}\Sigma(\mathbf{k}, E + i\eta) + i\text{Im}\Sigma(\mathbf{k}, E + i\eta)$  is the self-energy of interacting electrons. T(E) is the so-called T-matrix, representing the possible scattering processes between states  $|\mathbf{k}\rangle$  and  $|\mathbf{k} + \mathbf{q}\rangle$  for a point like s-wave scatterer. Atomic scale imaging of these interference patterns  $\delta N(\mathbf{r}, E)$  is achieved using spatial mapping of the differential conductance,  $g(\mathbf{r}, E)^{14}$ .

#### **Results**

### Modeling the $(\pi,\pi)$ orbital order

As a concrete model, we consider orbital order of  $d_{xz}/d_{yz}$ -orbitals on a 2D square-lattice (Fig. 1a). To accommodate the  $(\pi,\pi)$  orbital order, the unit cell is enlarged to a two-sublattice basis allowing for the incorporation of a staggered, nematic orbital order preserving the translational and global  $C_4$ -symmetry. Including superconductivity the model Hamiltonian takes the form,

$$H = \sum_{\mathbf{k}} \psi_{\mathbf{k}}^{\dagger} \begin{pmatrix} \mathcal{H}_{0}(\mathbf{k}) + \mathcal{H}_{oo}(\mathbf{k}) & \Delta_{d}(\mathbf{k}) \\ \Delta_{d}^{\dagger}(\mathbf{k}) & -\mathcal{H}_{0}^{*}(-\mathbf{k}) - \mathcal{H}_{oo}^{*}(-\mathbf{k}) \end{pmatrix} \psi_{\mathbf{k}}, \tag{2}$$

where the Nambu spinor is defined as

$$\psi_{\mathbf{k}}$$
 =

$$\left(c_{A,xz,\uparrow}(\mathbf{k}),c_{A,yz,\uparrow}(\mathbf{k}),c_{B,xz,\uparrow}(\mathbf{k}),c_{B,yz,\uparrow}(\mathbf{k}),c_{A,xz,\downarrow}^{\dagger}(-\mathbf{k}),c_{A,yz,\downarrow}^{\dagger}(-\mathbf{k}),c_{B,xz,\downarrow}^{\dagger}(-\mathbf{k}),c_{B,yz,\downarrow}^{\dagger}(-\mathbf{k})\right)^{T}$$

with  $c_{\nu,\mu,\sigma}(\mathbf{k})$  annihilating an electron with momentum  $\mathbf{k}$  and spin  $\sigma$ at sublattice  $\nu$  in orbital  $d_{\mu}$ . Here  $\mathcal{H}_0(\mathbf{k})$  contains intra- and interorbital nearest- and next-nearest-neighbour hoppings allowed by the d-wave symmetry of the orbitals,  $\mathcal{H}_{oo}(\mathbf{k})$  introduces the on-site anti-ferro-orbital order and  $\Delta_{\mathbf{d}}(\mathbf{k})$  contains nearest- and next-nearest-neighbour intraorbital d-wave pairings as introduced in Ref. 15. Here for generality we consider the simplest model Hamiltonian ( $\mathcal{H}_0(\mathbf{k}), \mathcal{H}_{oo}(\mathbf{k})$ ) rather than specific Hamiltonian of CeCoIn<sub>5</sub>. As the model is spin-independent we suppress the spin index below. To separate the energy scales of the orbital and superconducting orders, the orbital order is introduced at an energy scale well above the superconducting gap, i.e.  $\Delta_{oo} \gg \Delta_{d}$ . The Hamiltonian in (2) is chosen as a minimal model approach where  $\mathcal{H}_0(\mathbf{k})$  describes the simplest band dispersion allowing for the implementation of local  $C_4$ -symmetry breaking. A detailed description of the model and parameters can be found in SI Section 1.

To simulate QPI, a non-magnetic impurity is introduced as a point-like potential. We choose an on-site impurity as the scattering center, because this kind of impurity widely exists in the crystals and is located at a high symmetry point required to detect the local symmetry breaking caused by the orbital order. The impurity, either a different element or lattice vacancy, is assumed to exhibit a trivial spatial structure leading to identical potential strengths in the orbital degree of freedom. The local density of states (LDOS) is computed using a T-matrix approach as

$$N(\mathbf{R}, \gamma, E) = -\frac{1}{\pi} \operatorname{Im} \left( G^{\mathbf{R}}(\mathbf{0}, E) + G^{\mathbf{R}}(\mathbf{R}, E) T(\mathbf{0}, E) G^{\mathbf{R}}(-\mathbf{R}, E) \right)_{\gamma\gamma}$$
(3)

where  $\mathbf{R}$  is the real-space position of the two-ion unit cell,  $\gamma \in \{v = A, B; \mu = xz, yz\}$ , the T-matrix is given by  $T(\mathbf{0}, E) = \left[1 - H_{imp}(\mathbf{0})G^R(\mathbf{0}, E)\right]^{-1}H_{imp}(\mathbf{0})$  and  $G^R(\mathbf{R}, E) = G^0(\mathbf{R}, i\omega_n \to E + i\eta) = \sum_{\mathbf{k}} e^{i\mathbf{k}\cdot\mathbf{R}}G^0(\mathbf{k}, i\omega_n)$  is the bare, retarded Greens function obtained from (2). We always insert the impurity at one of the two sites in the unit cell positioned at  $\mathbf{R} = \mathbf{0}$  for simplicity. Note that  $N(\mathbf{R}, \gamma, E)$  contains four components for the unit cell at  $\mathbf{R}$ , corresponding to the orbital and sublattice degrees of freedom. The position of a single lattice site,  $\mathbf{r}$ , is uniquely mapped from the set  $\{\mathbf{R}, \nu\}$  enabling a straightforward transition to the site-resolved LDOS. To allow for reliable comparison to experimental data, we calculate the local density of states above the surface of the material following a simplified method that takes the Wannier orbitals into account  $^{16,17}$  and basically weigh the computed  $N(\mathbf{r}, E)$  by atomic-like  $d_{xz}/d_{yz}$  orbitals. To account for the experimental resolution of 100  $\mu$ eV, we perform an additional Gaussian energy convolution, details on these calculations can be found in SI Section 2.

## Consequences for QPI of $(\pi,\pi)$ orbital order

The consequences of this  $(\pi,\pi)$  orbital order for QPI experiments are intriguing. Surprisingly, theoretical modeling for the **r**-space QPI patterns,  $N(\mathbf{r}, E)$ , around the impurity at sublattice  $\boldsymbol{a}$  (Fig. 2a) and sublattice  $\boldsymbol{b}$  (Fig. 2d) at energy  $|E| > \Delta$  well outside the superconducting gap, show almost identical  $N(\mathbf{r}, E)$ . At energies  $|E| < \Delta$ , however, the situation is radically different. Here  $N(\mathbf{r}, E)$  around chemically identical impurity atoms at sublattice  $\boldsymbol{a}$  (Fig. 2b) and sublattice  $\boldsymbol{b}$  (Fig 2e) are vividly different. The key consequence is

that the amplitude of scattering interference is far more intense along one axis than along the other axis, depending on which sublattice the impurity atom resides. The interference pattern breaks C<sub>4</sub>-rotational symmetry, indicating the existence of the hidden  $(\pi,\pi)$  orbital order which breaks C<sub>4</sub>-symmetry locally. We stress that the impurity potential itself is pointlike and of identical strength on both orbitals. The C<sub>4</sub>-symmetry breaking takes place because the impurity chooses a specific sublattice, in conjunction with the underlying orbital order. To quantify this local symmetry breaking effect, we define a dimensionless value  $A(\mathbf{r}, E) =$  $(N(\mathbf{r},E)-N^{\odot 90}(\mathbf{r},E))/(N(\mathbf{r},E)+N^{\odot 90}(\mathbf{r},E))$  as the local anisotropy, in which  $N^{\odot 90}(\mathbf{r},E)$ is 90-degree anti-clockwise-rotated  $N(\mathbf{r}, E)$  surrounding the impurity site at sublattice a/b. The  $A(\mathbf{r}, E)$  maps (Fig. 2c,f) at energies  $|E| < \Delta$  explicitly demonstrate the C<sub>4</sub>-symmetry breaking for both impurity positions. The maximum  $A(\mathbf{r}, E)$  value approaches 20%. Meanwhile, at the energy  $|E| > \Delta$ , still within the energy scale of the orbital order  $(\Delta_{00})$ ,  $A(\mathbf{r}, E)$  is less than 2% (Fig.S2). Thus, the orbital order can be clearly unraveled below the energy scale of the superconducting order parameter because of the opening of the superconducting gap selectively enhances its visibility. For comparison, the QPI simulation of the normal-state model at the energies  $|E| < \Delta$  can be seen Fig.S3, which is equivalent to the  $|E| > \Delta$  case of the superconducting model.

#### QPI signature of $(\pi,\pi)$ orbital order in CeCoIn<sub>5</sub>

To explore these predictions we studied CeCoIn<sub>5</sub>, a prototypical heavy-fermion superconductor, whose crystal unit cell has dimensions  $a=b=4.6\text{\AA}$ ,  $c=7.51\text{\AA}$  and with superconducting critical temperature  $T_c=2.3\text{K}$  (Ref. 18). As revealed by heavy-fermion scattering interference imaging, its Fermi surface is formed by two heavy bands ( $\alpha$  and  $\beta$  bands in Fig. 1b) due to the hybridization of a conventional light conduction band and the localized f-electrons<sup>19</sup>. In the superconducting state, the Cooper pairs are spin-singlets<sup>20,21</sup> and a Cooper pairing energy gap with apparent nodes  $|\Delta_{\alpha}(\mathbf{k})| = 0$  oriented along the  $\mathbf{k} = [(1,1); (1,-1)]2\pi/a$  directions<sup>21,22,23,24,25</sup> and a nodal, V-shaped  $N(E) \propto E$  with gap edges  $600\pm 50~\mu\text{eV}$ . The  $|\Delta_{\alpha}(\mathbf{k})|$  measured in  $\mathbf{k}$ -space with QPI is shown in Fig. 1c<sup>19</sup>. Our CeCoIns single crystal samples are inserted into the spectroscopic imaging STM, cleaved in cryogenic ultra-high vacuum, inserted into the STM head and cooled to T=280 mK.

A standard Co terminated surface topography  $T(\mathbf{r})$  is shown in Fig. 3a with sublattices marked by red dots and blue dots, respectively. The Co terminated surface is identified from both the tunneling conductance spectrum and the domain boundaries (SI section4). In this field of view (FOV), we find two single atom defects allocated at sublattice **a** and **b**, respectively. These two defects are nearly identical in topography image (Fig. 3a). Figure 3b shows simultaneously measured differential conductance map  $q(\mathbf{r}, E)$  at E=-0.94meV ( $|E| > \Delta$ ). Virtually, no difference in scattering interferences from defects in the different sublattices can be detected. In contrast, the simultaneously measured differential conductance map  $g(\mathbf{r}, E)$  at E=0 in the same FOV shown in Fig. 3c reveals highly distinct interference patterns. The scattering interference of one defect is far more intense along the  $\boldsymbol{a}$  axis than the  $\boldsymbol{b}$  axis, and vice versa. Indeed, they appear to be rotated by 90-degrees relative to each other, in agreement with the theoretical prediction in Fig. 2. Furthermore, Fig. S5 gives the comparison of  $A(\mathbf{r}, E)$  surrounding the same defect in the superconducting state ( $T < T_c$ ) (Fig. S5a,b,c) and in the normal state( $T > T_c$ ) (Fig. S5d,e,f). The local anisotropy  $A(\mathbf{r}, E)$  is only enhanced at E=0 in the superconducting state while has no apparent change at E=0 in the normal state, in agreement with the theoretical prediction in Fig. S4.

Next, we study the local anisotropy  $A(\mathbf{r}, E)$  around the defects at the two sublattices. Figure 4a,d contain the measured local anisotropy  $A(\mathbf{r}, E)$  at E=0 around the defects at sublattice  $\mathbf{a}$  (Fig. 4a) and sublattice  $\mathbf{b}$  (Fig. 4d). Obviously, the conductance anisotropy is rotated by 90-degrees for scattering centres at the different sublattice sites. To analyse the energy-dependence of  $A(\mathbf{r}, E)$  we plot in Fig. 4b,e, the line profiles of  $A(\mathbf{r}, E)$  along the high symmetry directions (0,1) and (1,0) versus bias. The anisotropy is very weak (light blue and light red) at the energies outside the superconducting gap, while, inside the superconducting gap, the anisotropy rapidly increases (dark blue and dark red) and its maxima are indistinguishable from  $E\sim0$ . Moreover, the curves of  $A(\mathbf{r}, E)$  at the second atom site away from the defect center (region marked by black squares in Fig. 4a,d) also exhibits this property (Fig. 4c, f). For comparison, we plot the theoretical curve of  $A(\mathbf{r}, E)$  along the same

high symmetry directions at each energy in Fig. S4. The theory curve features the same tendency as the experimental curve that  $A(\mathbf{r}, E)$  is significantly enhanced inside the superconducting gap and the maximum of  $A(\mathbf{r}, E)$  is indistinguishable from  $E \sim 0$ .

Finally, we use a multi-atom (MA) averaging technique resolved by sublattice to establish the repeatability of these phenomena for all equivalent impurity atoms. Figure 5a,b and 5e,f indicate the scattering centers at sublattice a (Fig. 5a,b) and sublattice b (Fig. 5e,f) marked by red circles that are involved in the MA analysis. The MA technique averages the over several defects located at the mapping data same sublattice <sup>26</sup>. Since multiple sites are averaged, the random local distortion and noise are suppressed, and the common feature surrounding the defects is enhanced (SI Section 3). Figures 5c,g present the MA-averaged topography and differential conductance map  $g_{MA}(\mathbf{r}, E)$  at E=0 for impurity atoms on sublattice a and b, respectively. The similar features seen in MA-averaged differential conductance map  $g_{MA}(\mathbf{r}, E)$  (Fig. 5c,g) and single-defect differential conductance map  $g(\mathbf{r}, E)$  (Fig. 3c) reveals that the scattering interferences from the two sublattices are highly distinct and repeatably rotated by 90-degrees relative to each other. One advantage of the MA process is that, since the random features in the mapping image are suppressed, the averaged image can be regarded as a single defect that resides in a defect-free large FOV, even though the actual sample is defective. This advantage allows us to Fourier transform the interference signal surrounding the single defect with high resolution in  $\mathbf{q}$ -space. We set the real-space origin  $(\mathbf{r} = \mathbf{0})$  at the defect site and focus on the real part of Fourier transformed map  $g_{MA}(\mathbf{q}, E)$  (Fig. 5d,h), as our defects are symmetric under the inversion operation and the real part of Fourier terms represent centrosymmetric cosine waves in rspace. Again, Re( $g_{MA}(\mathbf{q}, E)$ ) of the defects at different sublattice  $\mathbf{a/b}$  is also related to each other by a 90-degree rotation. Remarkably, several features of  $Re(g_{MA}(\mathbf{q}, E))$ , for example the distribution of the positive (blue) and negative (red) values, are reproduced by our theory (Fig. S7). Note that our theoretical model is based on a simple band dispersion, as described in SI Section 1.

#### **Discussion**

In this work we have explored the QPI signatures of  $(\pi,\pi)$  orbital order in CeCoIn<sub>5</sub>. The subtlety of such orders is in their preservation of crystal lattice symmetries which makes them undetectable by traditional scattering techniques<sup>8,9</sup>. On the other hand, pioneering STM visualization studies of anisotropic electron density due to orbital order has been reported<sup>27,10</sup>. Such experiments must be carried out under extreme tunneling conditions, for example at currents >10nA that, according to the Tersoff-Hamann theory <sup>28</sup>, require a miniscule tip-sample distance. Such tip-surface distances usually challenge the stability of the STM junction and, moreover, the tip-sample interaction may then become so intense as to alter the sample properties. By contrast, taking CeCoIn<sub>5</sub>  $(\pi, \pi)$  orbital order as an example, we have explored the possibility of using conventional junction QPI to detect the local symmetry breaking orbital order. From theory, it was predicted that, even with an isotropic impurity, the underlying orbital order should reveal itself as a sublattice-selective anisotropy in the surrounding QPI pattern, due to the different effective coupling of the impurity to the two orbitals. This is because although the impurity is described as a simple point like potential with no spatial or orbital structure, the scattering T-matrix reflects the orbital order. This suggests strongly that the specific type of impurity is irrelevant to the overall conclusions. While the anisotropy of the scattering interferences is found to be essentially indiscernible in the normal electron state outside the superconducting gap, it is significantly enhanced at energies within the superconducting gap. This finding suggested an interesting effect where the energy scale of QPI experiments used in detection of hidden orbital order is governed by the superconducting gap energy, despite the energy scale of the underlying orbital being much larger. To investigate the prediction experimentally, we performed STM measurement on CeCoIn<sub>5</sub>, which yields remarkable agreement with the theory. Given our minimal model approach, where only  $d_{xz/yz}$ -orbitals are considered alongside the anti-ferro-orbital order, superconductivity and a point like impurity, the agreement with the experimental data is striking and suggests that the methods may be applicable to a range of superconducting materials exhibiting hidden order<sup>29</sup>.

#### **Methods**

### **Experiments**:

Single crystals of CeCoIn<sub>5</sub> were synthesized from an In flux by combining stoichiometric amounts of Ce and Co with excess In an alumina crucible and encapsulating the crucible in an evacuated quartz ampoule(details in ref. 30). Its superconductivity and electronic structure were studied in the previous work with  $T_c = 2.3K$  and  $\Delta = 600 meV^{19}$ . The samples were cleaved in ultrahigh vacuum at 10K before inserted into STM. All data are measured by etched tungsten tips with an energy-independent density of states. A standard lock-in amplifier was used for measuring scanning tunneling spectra. See Supplementary Information for additional details on data treatment and extraction.

## Theory:

The two-dimensional square lattice including staggered orbital order and superconductivity has been modelled by the Bogoliubov-de Gennes Hamiltonian in Equation (1). Simulations of the sublattice-selective Bogoliubov quasiparticle interference have been performed using a T-matrix approach, where a Fourier transformation of (1) allows for a computation of the real-space local density of states (LDOS) in the presence of an impurity using  $N(R, \gamma, E) = -\frac{1}{\pi} Im(G^R(\mathbf{0}, E) + G^R(R, E)T(\mathbf{0}, E)G^R(-R, E))_{\gamma\gamma}$ . The impurity was assumed to be non-magnetic with a trivial spatial structure (i.e. point-like). For comparison to experiment all computed N(r, E) are weighed by atomic-like  $d_{xz}/d_{yz}$  orbitals and an energy convolution was performed to model the finite experimental energy resolution. Finally, the quasiparticle interference anisotropy was obtained as  $A(r, E) = (N(r, E) - N^{O90}(r, E))/(N(r, E) + N^{O90}(r, E))$ . The LDOS anisotropy is strongly enhanced within the superconducting gap as evident from Fig. S4. The full model, all input parameters and further details of the calculations can be found in Supplementary Information Sections 1 and 2.

**Data Availability** All data are available in the main text on Zenodo <sup>31</sup>. Additional information is available from the corresponding author upon reasonable request.

**Code availability** The simulation code are provided on Zenodo<sup>31</sup>. The data analysis codes used in this study are available from the corresponding author upon reasonable request.

**Author Information** Correspondence and requests for materials should be addressed to B.M.A. <a href="mailto:bma@nbi.ku.dk">bma@nbi.ku.dk</a> and J.C.S.D. <a href="mailto:jcseamusdavis@gmail.com">jcseamusdavis@gmail.com</a>.

#### References

- 1 Georges, A., de' Medici, L. & Mravlje, J. Strong Correlations from Hund's Coupling. *Annual Review of Condensed Matter Physics* **4**, 137-178, doi:10.1146/annurev-conmatphys-020911-125045 (2013).
- 2 de'Medici, L. The Physics of Correlated Insulators, Metals, and Superconductors Modeling and Simulation Vol. 7 Forschungszentrum Juelich, pp 377-398, E. Pavarini, E. Koch, R. Scalettar, and R. Martin (eds.) (2017).
- 3 Sprau, P. O. *et al.* Discovery of orbital-selective Cooper pairing in FeSe. *Science* **357**, 75-80, doi:10.1126/science.aal1575 (2017).
- 4 Hu, H., Yu, R., Nica, E. M., Zhu, J.-X. & Si, Q. Orbital-selective superconductivity in the nematic phase of FeSe. *Physical Review B* **98**, 220503, doi:10.1103/PhysRevB.98.220503 (2018).
- 5 Bi, X. *et al.* Orbital-selective two-dimensional superconductivity in 2H-NbS<sub>2</sub>. *Physical Review Research* **4**, 013188, doi:10.1103/PhysRevResearch.4.013188 (2022).
- 6 Fernandes, R. M., Chubukov, A. V., Knolle, J., Eremin, I. & Schmalian, J. Preemptive nematic order, pseudogap, and orbital order in the iron pnictides. *Physical Review B* **85**, 024534, doi:10.1103/PhysRevB.85.024534 (2012).
- 7 Fernandes RM, Coldea AI, Ding H, Fisher IR, Hirschfeld PJ, Kotliar G. Iron pnictides and chalcogenides: a new paradigm for superconductivity. *Nature* **601**, 35-44 (2022).
- 8 Fink, J., Schierle, E., Weschke, E. & Geck, J. Resonant elastic soft x-ray scattering. *Reports on Progress in Physics* **76**, 056502, doi:10.1088/0034-4885/76/5/056502 (2013).
- 9 Ishihara, S. in *Resonant X-Ray Scattering in Correlated Systems* (eds Youichi Murakami & Sumio Ishihara) 1-45 (Springer Berlin Heidelberg, 2017).
- 10 Kim, H. et al. Atomic-scale visualization of surface-assisted orbital order. *Science Advances* **3**, eaao0362, doi:10.1126/sciadv.aao0362 (2017).
- 11 Kostin A, et al. Imaging orbital-selective quasiparticles in the Hund's metal state of FeSe. *Nature Materials* **17**, 869-874 (2018).
- 12 Wang, Q.-H. & Lee, D.-H. Quasiparticle scattering interference in high-temperature superconductors. *Physical Review B* **67**, 020511, doi:10.1103/PhysRevB.67.020511 (2003).

- 13 Capriotti, L., Scalapino, D. J. & Sedgewick, R. D. Wave-vector power spectrum of the local tunneling density of states: Ripples in a d-wave sea. *Physical Review B* **68**, 014508, doi:10.1103/PhysRevB.68.014508 (2003).
- 14 Bena, C. Friedel oscillations: Decoding the hidden physics. *Comptes Rendus Physique* **17**, 302-321, doi:https://doi.org/10.1016/j.crhy.2015.11.006 (2016).
- 15 Graser, S., Maier, T. A., Hirschfeld, P. J. & Scalapino, D. J. Near-degeneracy of several pairing channels in multiorbital models for the Fe pnictides. *New Journal of Physics* **11**, 025016, doi:10.1088/1367-2630/11/2/025016 (2009).
- 16 Choubey, P., Berlijn, T., Kreisel, A., Cao, C. & Hirschfeld, P. J. Visualization of atomic-scale phenomena in superconductors: Application to FeSe. *Physical Review B* **90**, 134520, doi:10.1103/PhysRevB.90.134520 (2014).
- 17 Kreisel, A. et al. Towards a quantitative description of tunneling conductance of superconductors: Application to LiFeAs. *Physical Review B* **94**, 224518, doi:10.1103/PhysRevB.94.224518 (2016).
- 18 Petrovic, C. *et al.* Heavy-fermion superconductivity in CeCoIn<sub>5</sub> at 2.3 K. *Journal of Physics: Condensed Matter* **13**, L337-L342, doi:10.1088/0953-8984/13/17/103 (2001)
- 19 Allan, M. P. *et al.* Imaging Cooper pairing of heavy fermions in CeCoIn<sub>5</sub>. *Nature Physics* **9**, 468-473, doi:10.1038/nphys2671 (2013).
- 20 Kohori, Y. *et al.* NMR and NQR studies of the heavy fermion superconductors CeTIn<sub>5</sub> (T = Co and Ir). *Physical Review B* **64**, 134526, doi:10.1103/PhysRevB.64.134526 (2001).
- 21 Curro, N. J. *et al.* Anomalous NMR magnetic shifts in CeCoIn<sub>5</sub>. *Physical Review B* **64**, 180514, doi:10.1103/PhysRevB.64.180514 (2001).
- 22 Movshovich, R. *et al.* Unconventional Superconductivity in CeIrIn<sub>5</sub> and CeCoIn<sub>5</sub>: Specific Heat and Thermal Conductivity Studies. *Physical Review Letters* **86**, 5152-5155, doi:10.1103/PhysRevLett.86.5152 (2001).
- 23 Izawa, K. *et al.* Angular Position of Nodes in the Superconducting Gap of Quasi-2D Heavy-Fermion Superconductor CeCoIn<sub>5</sub>. *Physical Review Letters* **87**, 057002, doi:10.1103/PhysRevLett.87.057002 (2001).
- 24 Stock, C., Broholm, C., Hudis, J., Kang, H. J. & Petrovic, C. Spin Resonance in the d-Wave Superconductor CeCoIns. *Physical Review Letters* **100**, 087001, doi:10.1103/PhysRevLett.100.087001 (2008).

- 25 An, K. *et al.* Sign reversal of field-angle resolved heat capacity oscillations in a heavy Fermion superconductor CeCoIn<sub>5</sub> and  $d_{x2-y2}$  pairing symmetry. *Physical Review Letters* **104**, 037002, doi:10.1103/PhysRevLett.104.037002 (2010).
- 26 Sharma, R. et al. Multi-atom quasiparticle scattering interference for superconductor energy-gap symmetry determination. *npj Quantum Materials* **6**, 7, doi:10.1038/s41535-020-00303-4 (2021).
- 27 Takahashi, Y. et al. Orbital Selectivity in Scanning Tunneling Microscopy: Distance-Dependent Tunneling Process Observed in Iron Nitride. *Physical Review Letters* **116**, 056802, doi:10.1103/PhysRevLett.116.056802 (2016).
- 28 Tersoff, J. & Hamann, D. R. Theory and Application for the Scanning Tunneling Microscope. *Physical Review Letters* **50**, 1998-2001, doi:10.1103/PhysRevLett.50.1998 (1983).
- 29 Chandra, P., Coleman, P., Mydosh, J. A. & Tripathi, V. Hidden orbital order in the heavy fermion metal URu<sub>2</sub>Si<sub>2</sub>. *Nature* **417**, 831-834, doi:10.1038/nature00795 (2002).
- 30 Petrovic, C. et al. Heavy-fermion superconductivity in CeCoIn<sub>5</sub> at 2.3 K. *J Phys-Condens Mat* **13**, L337-L342, doi: 10.1088/0953-8984/13/17/103 (2001).
- 31 Weijiong, C. et al. Replication Data for: Interplay of Hidden Orbital Order and Superconductivity in CeCoIn<sub>5</sub>, Zenodo https://doi.org/10.5281/zenodo.7859619 (2023)

**Acknowledgements**: J.C.S.D. acknowledges support from the Moore Foundation's EPiQS Initiative through Grant GBMF9457, from the European Research Council (ERC) under Award DLV-788932 and from Science Foundation of Ireland under Award SFI 17/RP/5445. W.C. and J.C.S.D. acknowledge support from the Royal Society under Award R64897. C. N. B., A.K. and B. M. A. acknowledge support by the Danish National Committee for Research Infrastructure (NUFI) through the ESS-Lighthouse Q-MAT. P. J. H acknowledges support from the Department of Energy under Grant No. DE-FG02-05ER46236. C. P. acknowledges support from the U.S. Department of Energy, Office of Basic Energy Science, Division of Materials Science and Engineering, under Contract No. DE-SC0012704 (materials synthesis).

**Author Contributions Statement:** W.C. and J.C.S.D. conceived the project. J.C.S.D., A.K. and B.M.A. supervised the research. C.P. synthesized and characterized the samples; F.M. and

M.P.A. carried out STM measurements. Theoretical analyses were carried out by C.N.B, P.J.H., B.M.A. and A.K. Experimental analysis was carried out by W.C. J.C.S.D. and B.M.A. wrote the paper with key contributions from A.K., C.N.B., P.J.H. and W.C. The manuscript reflects the contributions and ideas of all authors.

**Competing Interests Statement:** The authors declare no competing financial or non-financial interests.

## **Figure Legends**:

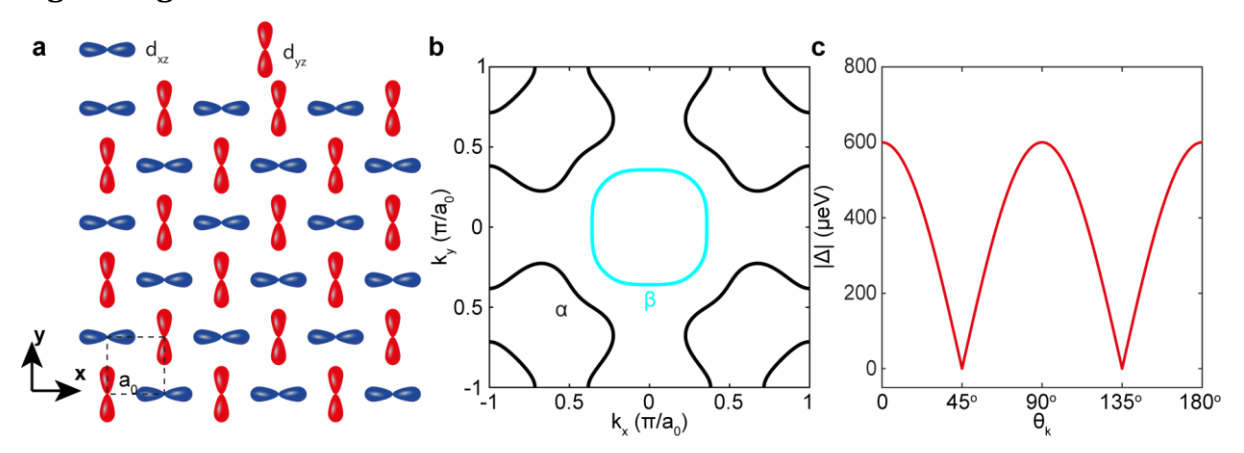


Figure 1.  $(\pi, \pi)$  orbital order on the surface of CeCoIn<sub>5</sub>

- a. Schematic of  $(\pi, \pi)$  orbital order on the surface of CeCoIn<sub>5</sub>. Two sublattices are introduced by the  $d_{xz}/d_{yz}$  orbital order.
- b. The Fermi surface of CeCoIn<sub>5</sub> measured by heavy-fermion quasiparticle interference<sup>19</sup>.
- c. Superconducting energy gap structure of CeCoIn<sub>5</sub> measured about the  $(\pi,\pi)$  point<sup>19</sup>. The order parameter is believed to exhibit  $d_{x^2-y^2}$  symmetry.

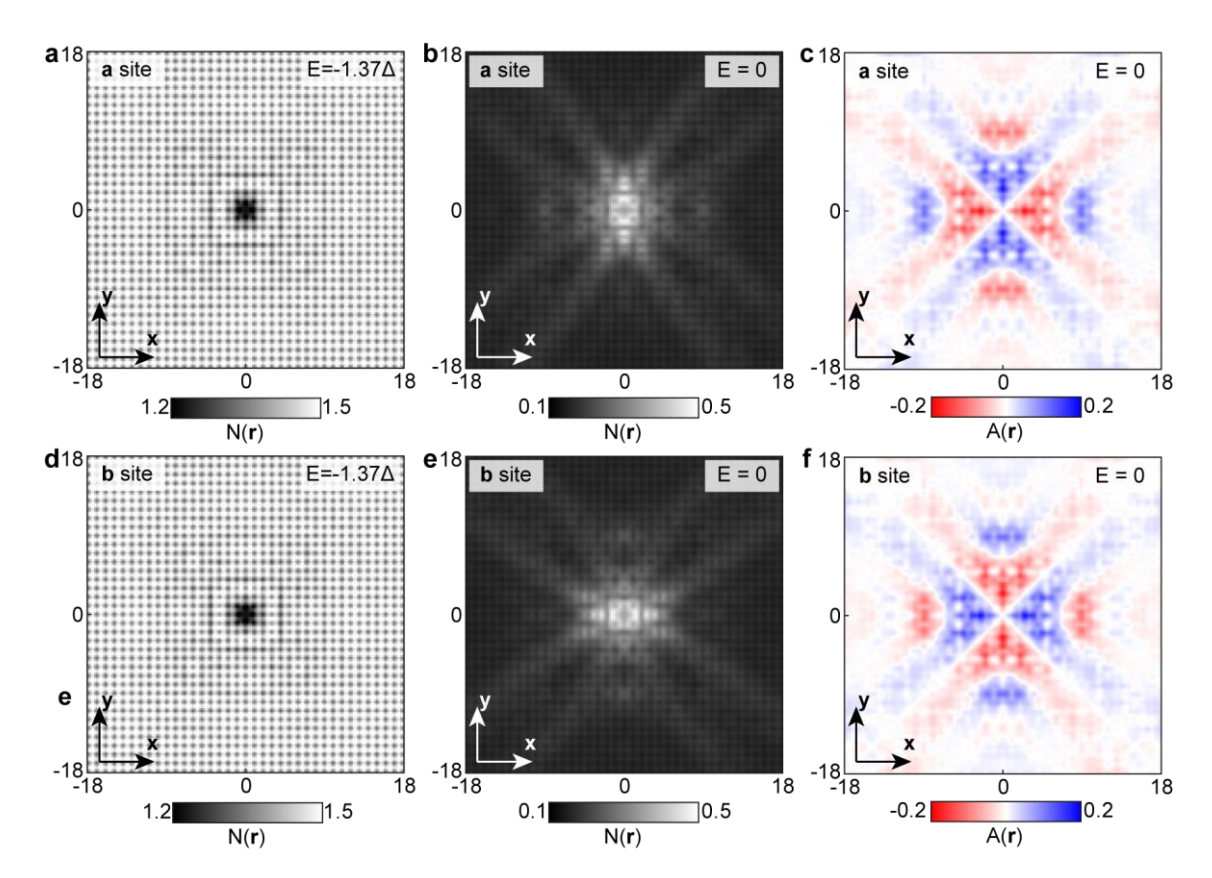


Figure 2. Bogoliubov quasiparticle interference from  $(\pi, \pi)$  orbital order calculated by the theoretical models

a,d. Theoretical results for BQPI pattern  $N(\mathbf{r}, E)$  with the impurity atom at sublattice  $\boldsymbol{a}$  (a) and sublattice  $\boldsymbol{b}$  (d) at the energy well outside the superconducting gap  $E > |\Delta|$ . b,e. Theoretical results for BQPI pattern  $N(\mathbf{r}, E)$  with the impurity atom at sublattice  $\boldsymbol{a}$  (b) and sublattice  $\boldsymbol{b}$  (e) at the energy well below the superconducting gap edge  $E < |\Delta|$ . The local anisotropy  $A(\mathbf{r}, E)$  with the impurity atom at sublattice  $\boldsymbol{a}$  (c) and sublattice  $\boldsymbol{b}$  (f) at the energy well below the superconducting gap edge  $E < |\Delta|$ .

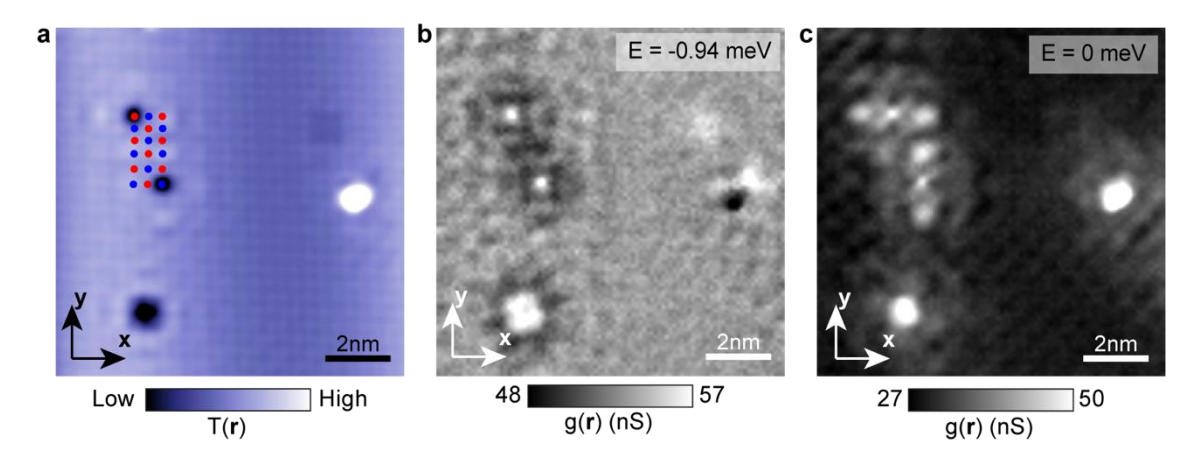


Figure 3. Example of QPI imaging resolved sublattices in CeCoIn<sub>5</sub>

- a. Atomic resolved topography image around two sublattices. Two sublattices are indicated schematically by red dots and blue dots, respectively. (setpoint: V = -10 meV, I = 800 pA)
- b. Simultaneous measured differential conductance map  $g(\mathbf{r}, E)$  at  $E = -0.94 \, meV$  in the FOV of image (a).
- c. Simultaneous measured differential conductance map  $g(\mathbf{r}, E)$  at E = 0 in the FOV of image (a). The BQPI patterns on the two sublattices are clearly distinct and appear to be rotated by 90-degrees relative to each other.

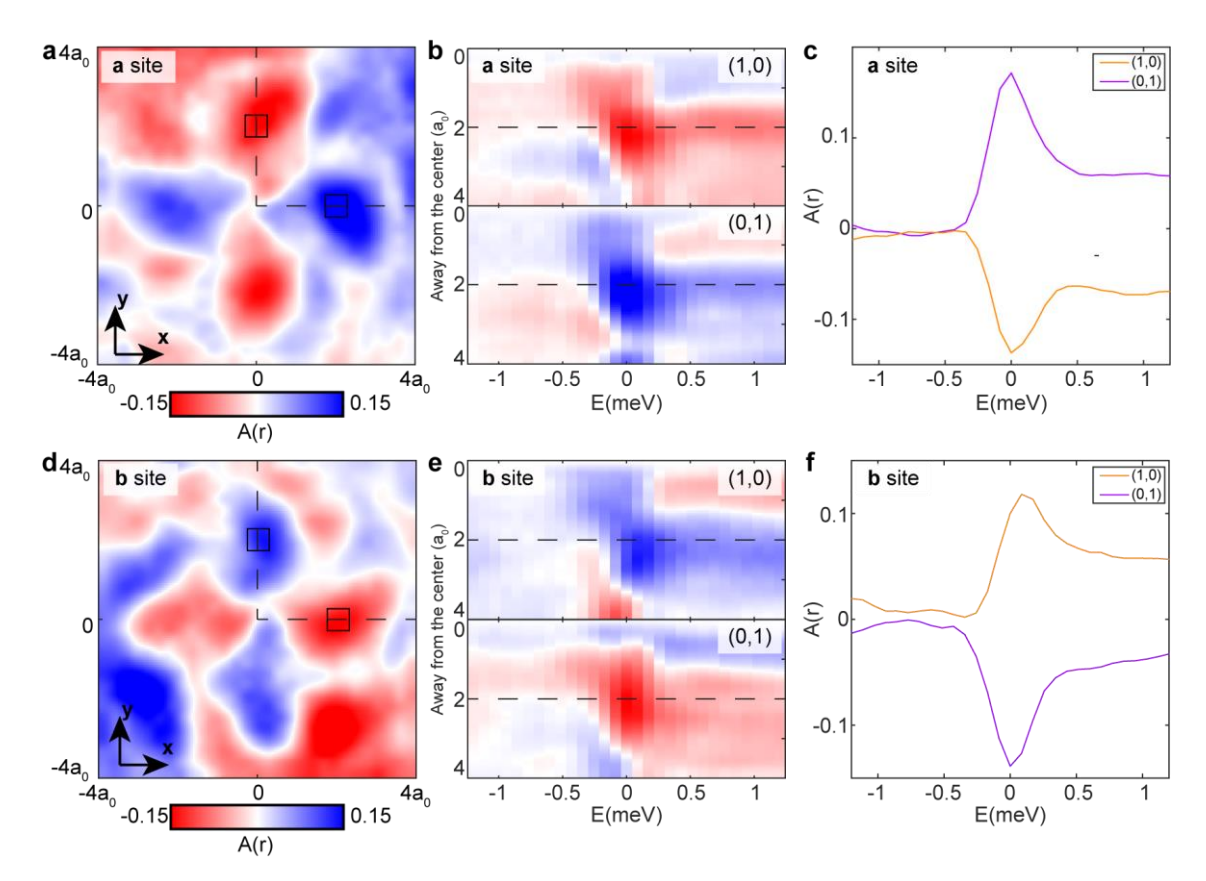


Figure 4. Local anisotropy A(r, E) around defects in two sublattices.

- a,d, Measured local anisotropy  $A(\mathbf{r}, E)$  around the defects at sublattice  $\mathbf{a}$  (a) and sublattice  $\mathbf{b}$  (e). The length scale of a, e is in the unit of lattice constant  $a_0$ .
- b,c, Measured local anisotropy  $A(\mathbf{r}, E)$  around the defects at sublattice  $\mathbf{a}$  (b) and sublattice  $\mathbf{b}$  (f) along the high symmetry direction (1,0) and (0,1) versus energy.
- c,f, Averaged local anisotropy  $A(\mathbf{r}, E)$  around the defects at sublattice  $\mathbf{a}$  (d) and sublattice  $\mathbf{b}$  (f) in region marked as black square in a and e and as black dashed lines in b,c,f,g versus energy. The energy maxima of the anisotropy are indistinguishable from  $E \sim 0$ .

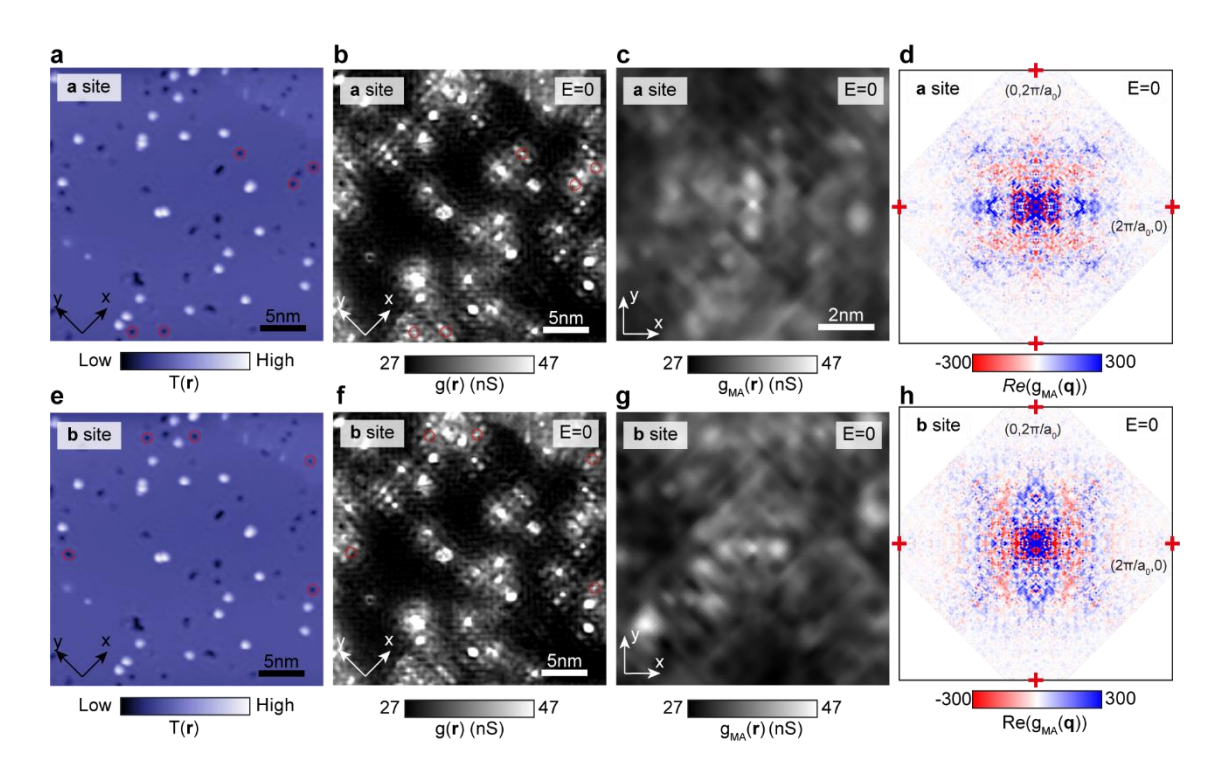


Figure 5. Multi-atom QPI analysis sampled by sublattice.

- a,e, Topography of the surface of CeCoIn<sub>5</sub>. (setpoint: V = -10 meV, I = 800 pA)
- b,f Differential conductance map  $g(\mathbf{q}, E)$  of the surface of CeCoIn<sub>5</sub>. The scattering centers at sublattice  $\mathbf{a}$  (a,b) and sublattice  $\mathbf{b}$  (e,f) are marked by red circles which are involved in the multi-atom analysis.
- c,g, Simultaneous MA-averaged differential conductance map  $g_{MA}(\mathbf{r}, E)$  at  $E \sim 0$  around the defects at sublattice  $\mathbf{a}$  (c) and sublattice  $\mathbf{b}$  (g).
- d.h, Real components of Fourier transformed MA-averaged differential conductance map  $\Re e(g_{MA}(\mathbf{q}, E))$  at  $E \sim 0$  around the defects at sublattice  $\boldsymbol{a}$  (e) and sublattice  $\boldsymbol{b}$  (h).

## Supplementary information for

# Interplay of Hidden Orbital Order and Superconductivity in CeCoIn<sub>5</sub>

Weijiong Chen, Clara Neerup Breiø, Freek Massee, M.P. Allan, C. Petrovic, J.C. Séamus Davis, P.J. Hirschfeld, B.M. Andersen and Andreas Kreisel

## 1. Theoretical Model of $(\pi, \pi)$ Orbital Order.

Our minimal 2D square-lattice model Hamiltonian  $\mathcal{H}_0(\mathbf{k})$  includes only electronic states of  $d_{xz}/d_{yz}$ -orbitals on each lattice point. The assumed band structure is similar to the one used in Ref. 1. We enlarge the unit cell to a two-ion basis allowing for the incorporation of a staggered, nematic orbital order ( $(\pi,\pi)$ ) orbital order) preserving the translational and global rotational symmetries as it can be seen in Fig. 1a. Defining the two-ion(sublattice), two-orbital basis as

 $c_{\mathbf{k},\sigma} = \left(c_{A,xz,\sigma}(\mathbf{k}), c_{A,yz,\sigma}(\mathbf{k}), c_{B,xz,\sigma}(\mathbf{k}), c_{B,yz,\sigma}(\mathbf{k})\right)^T$ , where  $c_{\nu,\mu}(\mathbf{k})$  annihilates an electron in orbital  $d_{\mu}$  on sublattice  $\nu$  with momentum  $\mathbf{k}$  and spin  $\sigma$ , we can write

$$\mathcal{H}_{0}(\mathbf{k}) = \begin{pmatrix} \epsilon_{3}(\mathbf{k}) - \mu & \epsilon_{4}(\mathbf{k}) & \epsilon_{1}(\mathbf{k}) + \epsilon_{2}(\mathbf{k}) & 0 \\ \epsilon_{4}(\mathbf{k}) & \epsilon_{3}(\mathbf{k}) - \mu & 0 & \epsilon_{1}(\mathbf{k}) - \epsilon_{2}(\mathbf{k}) \\ \epsilon_{1}^{*}(\mathbf{k}) + \epsilon_{2}^{*}(\mathbf{k}) & 0 & \epsilon_{3}(\mathbf{k}) - \mu & \epsilon_{4}(\mathbf{k}) \\ 0 & \epsilon_{1}^{*}(\mathbf{k}) - \epsilon_{2}^{*}(\mathbf{k}) & \epsilon_{4}(\mathbf{k}) & \epsilon_{3}(\mathbf{k}) - \mu \end{pmatrix}$$
(S1)

with

$$\epsilon_1(\mathbf{k}) = -\frac{1}{2}(t_1 + t_2) \left( 1 + e^{ik_x} + e^{-ik_y} + e^{i(k_x - k_y)} \right)$$
 (S2)

$$\epsilon_2(\mathbf{k}) = -\frac{1}{2}(t_1 - t_2) \left(1 - e^{ik_x} - e^{-ik_y} + e^{i(k_x - k_y)}\right)$$
 (S3)

$$\epsilon_3(\mathbf{k}) = -2t_3\left(\cos(k_x) + \cos(k_y)\right)$$
 (S4)

$$\epsilon_4(\mathbf{k}) = -2t_4 \left( \cos(k_x) - \cos(k_y) \right) \tag{S5}$$

We adopt the hopping parameters  $\{t_1,t_2,t_3,t_4\}=\{-1.0,1.3,-0.85,-0.85\}$  from Ref. 1 and set the chemical potential  $\mu=2.25|t_1|$  in all computations. In this basis, the  $(\pi,\pi)$  orbital order can formally be written as

$$\mathcal{H}_{oo}(\mathbf{k}) = \Delta_{oo} \, \mathbf{c}_{\mathbf{k},\sigma}^{\dagger} \, \mathbf{s}_3 \, \mathbf{c}_{\mathbf{k},\sigma} \tag{S6}$$

where  $s_i$  and  $\sigma_i$  (i = 1,2,3) are the Pauli matrices in sublattice and orbital space, respectively, and  $\Delta_{oo} = 0.25|t_1|$  is the orbital order parameter. Note that because of the  $s_3$  in (S6), exchanging the sign of  $\Delta_{oo}$  amounts to interchanging the sublattices.

To include superconductivity of  $d_{x^2-y^2}$ -symmetry in a multi-orbital setting, we follow the work performed by Graser  $et\ al.$  in Ref. 1, where the real space pairings arising from spin-fluctuations in the basis of the two relevant orbitals are computed. In the single-ion unit cell picture, the largest pairing amplitudes are the two nearest-neighbor (NN) bonds along the y-axis (x-axis) for the  $d_{xz}$ -orbital ( $d_{yz}$ -orbital) as well as all four NNN bonds in both orbitals. Interorbital pairings are negligible. Rewriting these six pairing terms of each orbital channel in momentum space and setting these identical on the sublattices yields

$$\Delta_{\mathbf{d}}(\mathbf{k}) = -\Delta_{1} \left( \left( e^{ik_{x}} + e^{-ik_{y}} \right) c_{A,xz,\uparrow}^{\dagger}(\mathbf{k}) c_{B,xz,\downarrow}^{\dagger}(-\mathbf{k}) + \left( e^{-ik_{x}} + e^{ik_{y}} \right) c_{B,xz,\uparrow}^{\dagger}(\mathbf{k}) c_{A,xz,\downarrow}^{\dagger}(-\mathbf{k}) \right.$$

$$\left. - \left( 1 + e^{i(k_{x} - k_{y})} \right) c_{A,yz,\uparrow}^{\dagger}(\mathbf{k}) c_{B,yz,\downarrow}^{\dagger}(-\mathbf{k})$$

$$\left. - \left( 1 + e^{-i(k_{x} - k_{y})} \right) c_{B,yz,\uparrow}^{\dagger}(\mathbf{k}) c_{A,yz,\downarrow}^{\dagger}(-\mathbf{k}) \right)$$

$$\left. - 2\Delta_{2} \left( \cos(k_{x}) \right.$$

$$\left. + \cos(k_{y}) \right) \sum_{\nu = A,B} \left( c_{\nu,xz,\uparrow}^{\dagger}(\mathbf{k}) c_{\nu,xz,\downarrow}^{\dagger}(-\mathbf{k}) - c_{\nu,yz,\uparrow}^{\dagger}(\mathbf{k}) c_{\nu,yz,\downarrow}^{\dagger}(-\mathbf{k}) \right)$$

$$(S7)$$

where  $\{\Delta_1, \Delta_2\} = \{0.025, 0.02\}$  is the pairing amplitude between first and second neighbors, respectively, and the spin-singlet structure is implicit. In this model,  $\Delta_{oo} \sim 3\Delta_d$ , is estimated from the experimental fact that orbital order on the surface of CeCoIn<sub>5</sub> exists even at 6 K while the superconducting temperature of CeCoIn<sub>5</sub> is 2.3K. We also calculate the anisotropy for  $\Delta_{oo} = 0.1 |t_1| \sim \Delta_d$  (Fig. S8). The results are qualitatively identical to the results shown in Fig. S4 for  $\Delta_{oo} = 0.25 |t_1|$ .

Defining the Nambu spinor as

$$\psi_{\mathbf{k}} = (c_{\mathbf{k},\uparrow}, c^{\dagger}_{-\mathbf{k},\downarrow})$$

$$= (c_{A,xz,\uparrow}(\mathbf{k}), c_{A,yz,\uparrow}(\mathbf{k}), c_{B,xz,\uparrow}(\mathbf{k}), c_{B,yz,\uparrow}(\mathbf{k}), c_{A,xz,\downarrow}^{\dagger}(-\mathbf{k}), c_{A,yz,\downarrow}^{\dagger}(-\mathbf{k}), c_{B,xz,\downarrow}^{\dagger}(-\mathbf{k}), c_{B,yz,\downarrow}^{\dagger}(-\mathbf{k}))^{T}$$
(S8)

and neglecting the spin degree of freedom, we can write the full Hamiltonian as

$$H = \sum_{\mathbf{k}} \psi_{\mathbf{k}}^{\dagger} \begin{pmatrix} \mathcal{H}_{0}(\mathbf{k}) + \mathcal{H}_{oo}(\mathbf{k}) & \Delta_{d}(\mathbf{k}) \\ \Delta_{d}^{\dagger}(\mathbf{k}) & -\mathcal{H}_{0}^{*}(-\mathbf{k}) - \mathcal{H}_{oo}^{*}(-\mathbf{k}) \end{pmatrix} \psi_{\mathbf{k}}$$
 (S9)

This minimal model Hamiltonian only includes the key ingredients of the orbital order, Co  $d_{xz}/d_{yz}$  orbits.

In this work, we only consider the simplest model Hamiltonian including staggered orbital order and it is not identical to the real Fermi surface of CeCoIn<sub>5</sub>. We do not discuss a more complete model including both Ce and In atoms and the superconductivity originating from Ce atoms, since such issues are both beyond the scope of our current work and not relevant to its conclusions. Nevertheless, as shown in Fig. S7, the overall pattern of the real part of BQPI is still present in a good agreement between the calculation and the experiment except some inconsistencies in the exact period of the Friedel oscillations. This implies that our model indeed captures the key ingredients of symmetry-breaking QPI induced by the orbital order.

## 2. Quasiparticle Interference Simulation of Two Sublattice Scatterings

The local density of states (LDOS) is computed using a T-matrix approximation as

$$N(\mathbf{R}, \gamma, E) = -\frac{1}{\pi} \operatorname{Im} \left( G^{R}(\mathbf{0}, E) + G^{R}(\mathbf{R}, E) T(\mathbf{0}, E) G^{R}(-\mathbf{R}, E) \right)_{\gamma\gamma}$$
(S10)

where  $\mathbf{R}$  is the real-space position of the two-ion unit cell,  $\gamma \in \{ \nu = A, B ; \mu = xz, yz \}$ , the T-matrix is given by  $T(\mathbf{0}, \mathbf{E}) = \left[ 1 - H_{\mathrm{imp}}(\mathbf{0}) G^{\mathbf{R}}(\mathbf{0}, \mathbf{E}) \right]^{-1} H_{\mathrm{imp}}(\mathbf{0})$  with

$$H_{\text{imp}}(\mathbf{0}) = V_{\text{imp}} \, \psi_{\mathbf{0}}^{\dagger} \, \tau_{3} \, \frac{1}{2} (s_{0} \pm s_{3}) \sigma_{0} \, \psi_{\mathbf{0}} = V_{imp} \sum_{\mathbf{k} \, \mathbf{k}'} \psi_{\mathbf{k}}^{\dagger} \, \tau_{3} \, \frac{1}{2} (s_{0} \pm s_{3}) \sigma_{0} \, \psi_{\mathbf{k}'}$$
 (S11)

where  $\tau_i$  (i = 1,2,3) are the Pauli matrices in Nambu space,  $s_0$  and  $\sigma_0$  are identity matrices in sublattice and orbital space, respectively, and the sign refers to the impurity position at sublattice  $\boldsymbol{a}(+)$  or  $\boldsymbol{b}(-)$ , and  $G^R(\mathbf{R},E) = \mathcal{G}^0(\mathbf{R},i\omega_n \to E+i\eta) = \sum_{\mathbf{k}} e^{i\mathbf{k}\mathbf{R}} \mathcal{G}^0(\mathbf{k},i\omega_n)$ . We set  $V_{\rm imp} = 10|t_1|$  and  $\eta = 0.001|t_1|$  in all simulations. The sublattice site resolved local density of state (LDOS),  $N(\tilde{\mathbf{r}},\boldsymbol{E})$ , is uniquely mapped from the set  $\{\mathbf{R},\nu\}$ .

To improve the direct comparison to experiment we implement two modifications to the calculated LDOS. First, we take into account that the tunnelling process to the STM tip is in the exponential limit, i.e. the STM tip is several Å above the surface and the tunnelling conductance is proportional to the local density of states at that position. For our model, we use extended, atomic-like orbitals to calculate the local density of states<sup>2,3</sup>

$$N(\mathbf{r}, E) = \sum_{\tilde{\mathbf{r}}, \mu} N(\tilde{\mathbf{r}}, \mu, E) |w_{\tilde{\mathbf{r}}, \mu}(\mathbf{r})|^2$$
 (S12)

where  $w_{\tilde{\mathbf{r}},xz(yz)}(\mathbf{r}) = \frac{xz(yz)}{r}e^{-\alpha r}$  are hydrogen-like  $d_{xz(yz)}$  orbitals and  $\mu = xz,yz$ . Note that we perform the  $\tilde{\mathbf{r}}$ -summation over a 5x5 grid and this approximation neglects off-

diagonal and non-local contributions of the lattice Green function which are expected to be small<sup>2</sup>. The vector  $\mathbf{r} = (\mathbf{x}, \mathbf{y}, \mathbf{z})$  is defined on this 5x5 grid for each atomic site and we use the parameters  $\{\mathbf{z}, \alpha\} = \{1.05a_0, 1/a_0\}$ . Second, to account for the finite energy resolution in experimental data, we introduce a Gaussian energy convolution

$$N(\mathbf{r}, E) = \sum_{E'} N(\mathbf{r}, E') f(E - E', \sigma)$$
 (S13)

with  $f(E-E',\sigma)=\frac{1}{\sigma\sqrt{2\pi}}e^{-\frac{1}{2}\left(\frac{E'-E}{\sigma}\right)^2}$ .  $\sigma=\Delta/12$  corresponds to the experimental energy resolution ~100meV. Fig. S1 gives the direct comparison between calculated LDOS N(E) and measured density of state g(E) far from the impurities and at the impurity/defect site to reveal that our choice of model parameters allows to describe the spectral properties of the impurities in the experiment. In Fig. S2 we present the anisotropy in real space (see main text) as calculated in the superconducting state showing that the anisotropy at zero energy (E=0) is much larger than at a finite energy above the superconducting gap. In contrast, Fig. S3 shows the corresponding result as obtained without superconducting order (normal state) where the anisotropy is very small for both E = 0 and at finite energy. As a consequence, the orbital order would be difficult to detect in this local probe. The same conclusions can be read off from Fig. S4 where the anisotropy is plotted as function of energy with and without superconducting order.

We point out that the authors of Ref. [4] report a similar symmetry-breaking QPI caused by the nematicity in the FeSeTe system. Their observation is distinct from our result in two aspects. First, the global QPI analysis they perform discovers the order that breaks overall crystal lattice symmetry but should not yield anti-ferro-orbital order which perserves the global C4 symmetry as in CeCoIn5. Second, the nematicity they discover is only observed in the non-superconductive state at high energy beyond the coherence peak. This is also distinct from our present picture where the anisotropy from orbital order is significantly enhanced within the superconductive quasiparticles below the superconducting gap.

## 3. Multi-atom Technique

The multi-atom technique<sup>5</sup> is overlapping and averaging the same type of defects to suppress the random noise and highlight the common features of the defects. we first identify the coordinates  $\mathbf{R}_i$  of the centers of the defects from the topography. The defects

are chosen in the topography by eye selecting only those of the same type as in Fig. 3 and 4, since they are well allocated at sublattice site a/b. Then, the selected defects at sublattice a/b are distinguished by the surrounding scattering pattern in  $g(\mathbf{q}, E=0)$ map.

Here we choose one defect as example. The chosen defects are marked by a red circle in Fig. 5a,e (topography) and 5b,f ( $g(\mathbf{q}, E=0)$ ). The exact coordinate  $\mathbf{R}_i = (x_i, y_i)$ for the center of the defect is figured out by calculating the center of mass of with intensity as the weights in the subsidence region around the impurity as seen in the topography. The shift operation is done in the **q**-space on Fourier transformed map  $T(\mathbf{q})$  and  $g(\mathbf{q}, E)$  by

$$T_i^{S}(\mathbf{q}) = e^{i\mathbf{q} \cdot \mathbf{R}_i} T(\mathbf{q})$$

$$g_i^{S}(\mathbf{q}, E) = e^{i\mathbf{q} \cdot \mathbf{R}_i} g(\mathbf{q}, E)$$
(S14)

$$g_i^{\mathcal{S}}(\mathbf{q}, E) = e^{i\mathbf{q} \cdot \mathbf{R_i}} g(\mathbf{q}, E) \tag{S15}$$

This step executes a shift with periodic boundary conditions. After the inverse Fourier transformation, the shifted data are shown in Fig. S6b,f. The defect is shifted to the center of the map. Finally, we overlap and average the shifted  $g_i^{\mathcal{S}}(\mathbf{r},E)$  of all defects and get MAaveraged image  $g_{MA}(\mathbf{r}, E)$ .

$$T_{MA}(\mathbf{r}) = \frac{\sum_{i=1}^{N} T_i^{S}(\mathbf{r})}{N}$$
 (S16)

$$g_{MA}(\mathbf{r}, E) = \sum_{i=1}^{N} g_i^{S}(\mathbf{r}, E) / N$$
 (S17)

 $T_{MA}(\mathbf{r})$  and  $g_{MA}(\mathbf{r}, E)$  at sublattice a(b) are shown in Fig. S6c,g(d,h).

## 4. Identification of Termination Surface

As reported by Ref. [6], three different cleaved surfaces can be found in CeCoIns: Co surface, CeIn surface and In<sub>2</sub> surface. We first rule out the In<sub>2</sub> surface because this surface is reconstructed. Both Co surface and CeIn surface show the same lattice constant ~4.6Å. Here, we identify our measured surface as Co surface by two observations.

First, Fig. S8 shows the measured scanning tunneling spectrum on our sample surface. The spectrum presents a dip at ~5meV corresponding to the heavy-fermion hybridization gap. This spectrum is exactly the same as the spectrum measured on Co surface in Ref. [7], except that our energy resolution is better. However, the spectrum of the CeIn surface in Ref. [7] displays that the density of states at -30meV is larger than that at 30meV, different from what we observed.

Second, since the orbital order breaks the equivalence of Co sites in sublattice  $\boldsymbol{a}$  and  $\boldsymbol{b}$ , two degenerate states should appear on the surface. At the interface of these two degenerate states, domain boundaries should form. Ref. [7] reports that the domain boundaries only appear on Co surface, implying that the orbital order occurs only on Co surface. We also observe many domain boundaries on our measured surface (Fig. S9), indicating our cleaved surface is Co-terminated.

Furthermore, Fig. S10 shows two nearby domains with several defects close to the domain boundary. In the  $g(\mathbf{r}, E=0)$  map (Fig. S10c) in the same field of view in Fig. S10a, we choose the same type of defects as in Figs. 3 and 5 (of the main text), which apparently break the local  $C_4$  symmetry in the superconducting state at E=0, two in the left domain (domain 1) and one in the right domain (domain 2). According to their local anisotropy, we can distinguish at which sublattice sites these defects are located, and extract the sublattice a/b site order in each domain (red and blue dot in Fig. S10d). On the other hand, in Fig. S10b, the arrangement of Co atoms near the domain boundary can be directly visualized after we adjusted the colormap limits. Finally, in Fig. S10d, we draw a schematic diagram of sublattice a/b orders near the domain boundary, combining both the arrangement of the atoms shown in Fig. S10b and the sublattice a/b site order in each domain extracted by Fig.S10c. It clearly shows that the sublattice a/b site order in the two domains are opposite. This confirms that the domain boundary indeed forms at the interface of two degenerate orbital order states.

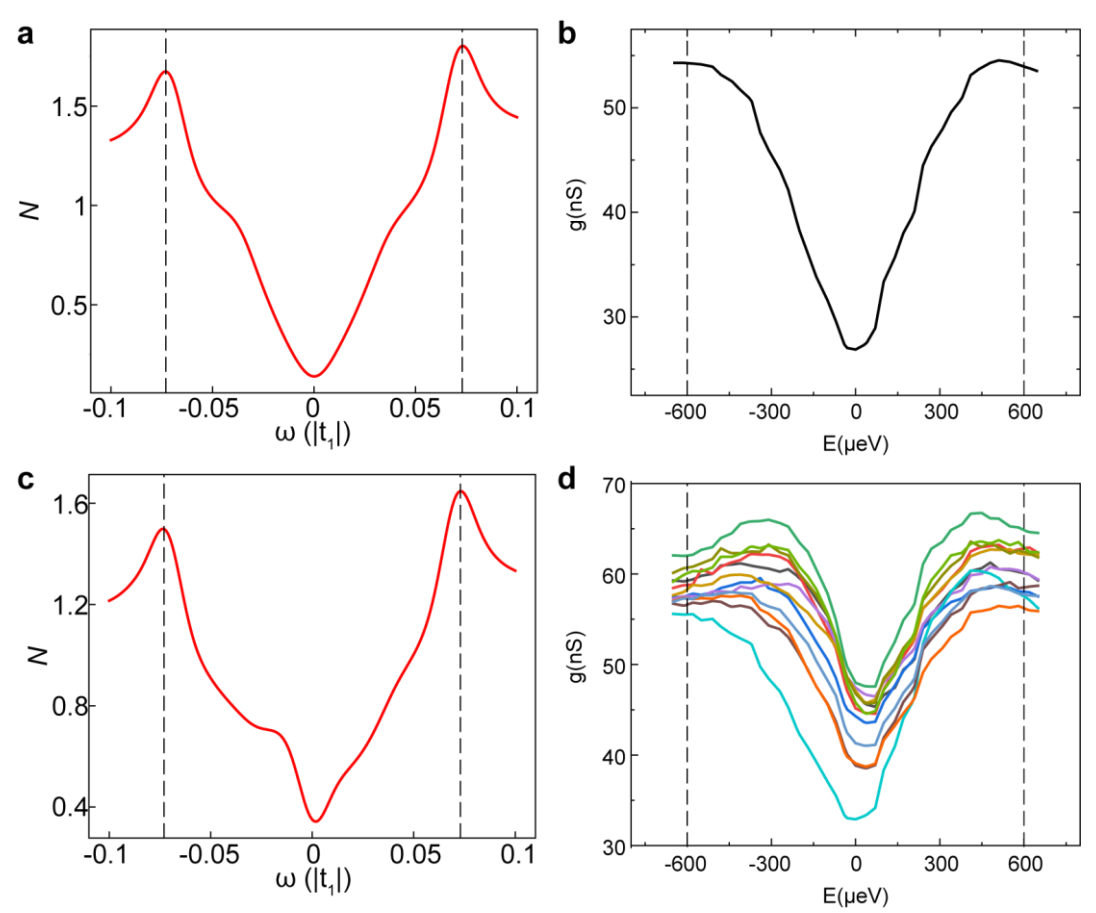


Figure S1. Simulated and measured spectra on the surface of CeCoIn<sub>5</sub>

- **a,b** Homogeneous spectra showing the V-shape signature of a  $d_{x^2-y^2}$  superconducting gap obtained from the simulation of our model with  $V_{imp} = 0.0$  (a) and measurement (b) at a site far from any impurities.
- $\mathbf{c}$ ,  $\mathbf{d}$  Simulated ( $\mathbf{c}$ ) and measured ( $\mathbf{d}$ ) spectra obtained at the impurity site positioned at either sublattice  $\mathbf{a}$  or  $\mathbf{b}$ .

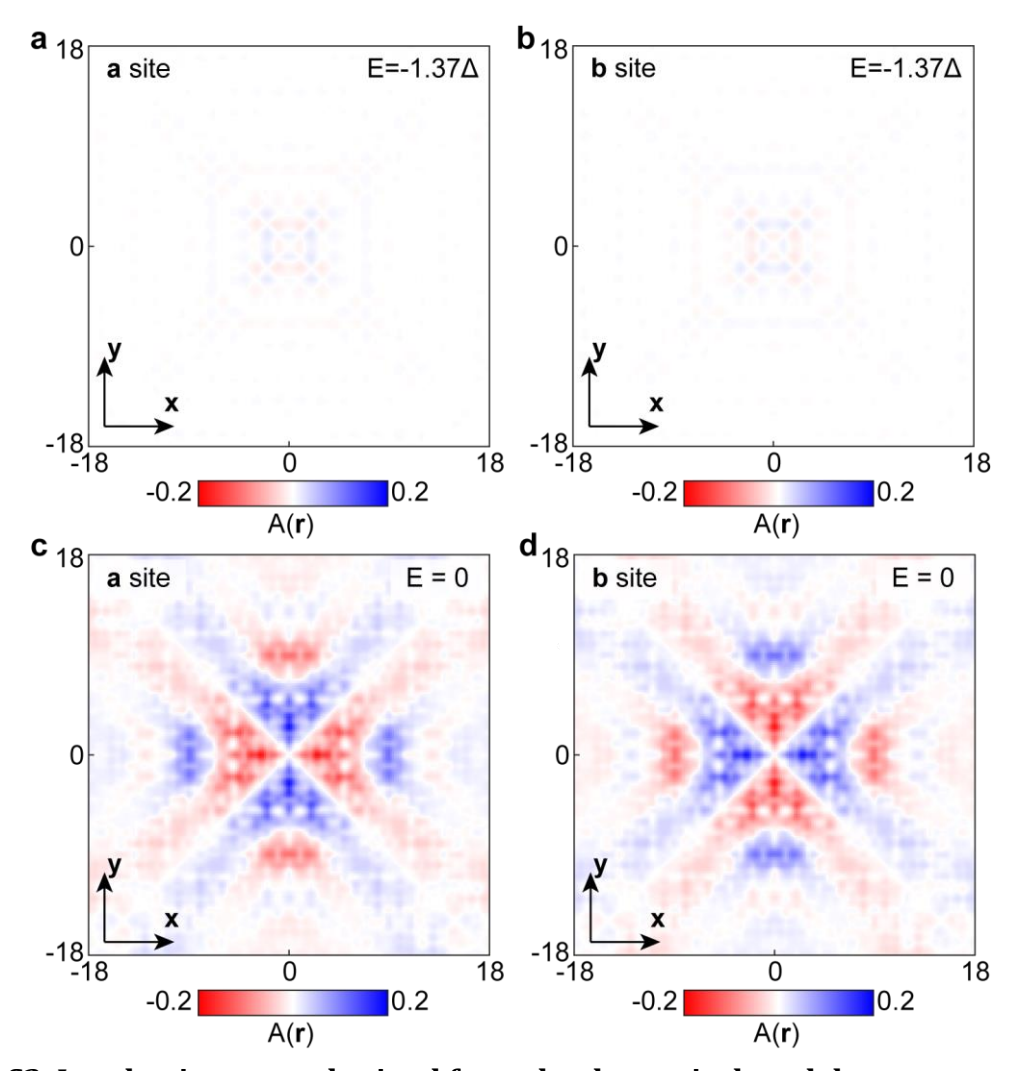


Figure S2. Local anisotropy obtained from the theoretical model

**a,b** The local anisotropy  $A(\mathbf{r}, E)$  with the impurity atom at sublattice  $\mathbf{a}$  (**a**) and sublattice  $\mathbf{b}$  (**b**) at the energy well above the superconducting gap  $E > |\Delta|$ . The local anisotropy  $A(\mathbf{r}, E)$  is no more than 2%.

**c,d** The local anisotropy  $A(\mathbf{r}, E)$  with the impurity atom at sublattice  $\mathbf{a}(\mathbf{c})$  and sublattice  $\mathbf{b}(\mathbf{d})$  at the energy well below the superconducting gap  $E < |\Delta|$ . Identical to Fig. 2c,f. The local anisotropy  $A(\mathbf{r}, E)$  approaches 20%.

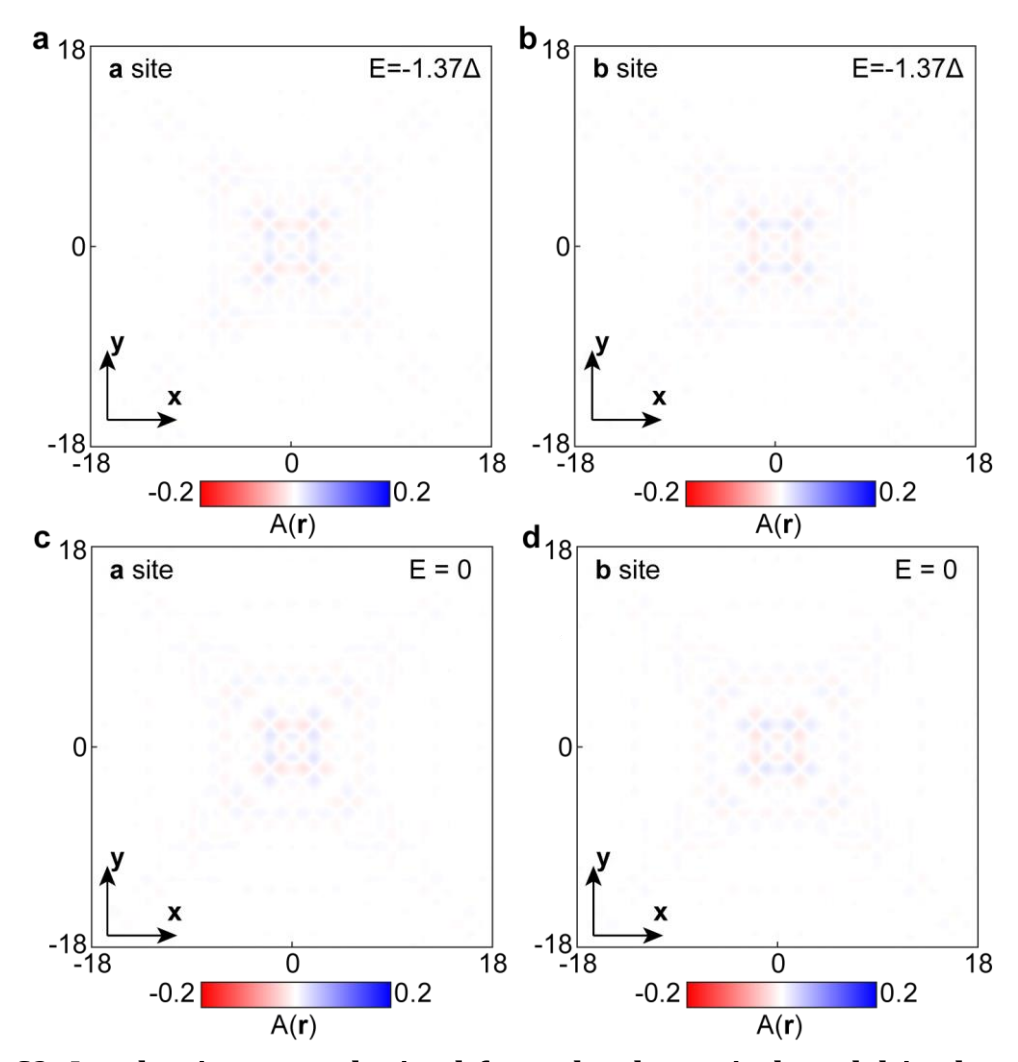


Figure S3. Local anisotropy obtained from the theoretical model in the normal state.

**a,b** The local anisotropy  $A(\mathbf{r}, E)$  in the normal state with the impurity atom at sublattice  $\mathbf{a}$  (a) and sublattice  $\mathbf{b}$  (b) at  $E > |\Delta|$ . Simulations computed by setting  $\{\Delta_1, \Delta_2\} = \{0.0, 0.0\}$ .

**c,d** The local anisotropy  $A(\mathbf{r}, E)$  in the normal state with the impurity atom at sublattice  $\mathbf{a}(\mathbf{c})$  and sublattice  $\mathbf{b}(\mathbf{d})$  at E=0. Simulations computed by setting  $\{\Delta_1, \Delta_2\} = \{0.0, 0.0\}$ . The local anisotropy  $A(\mathbf{r}, E)$  is less than 2% at both energies, similar to the simulation of the superconducting state at  $E > |\Delta|$  (Fig. S2 a,b).

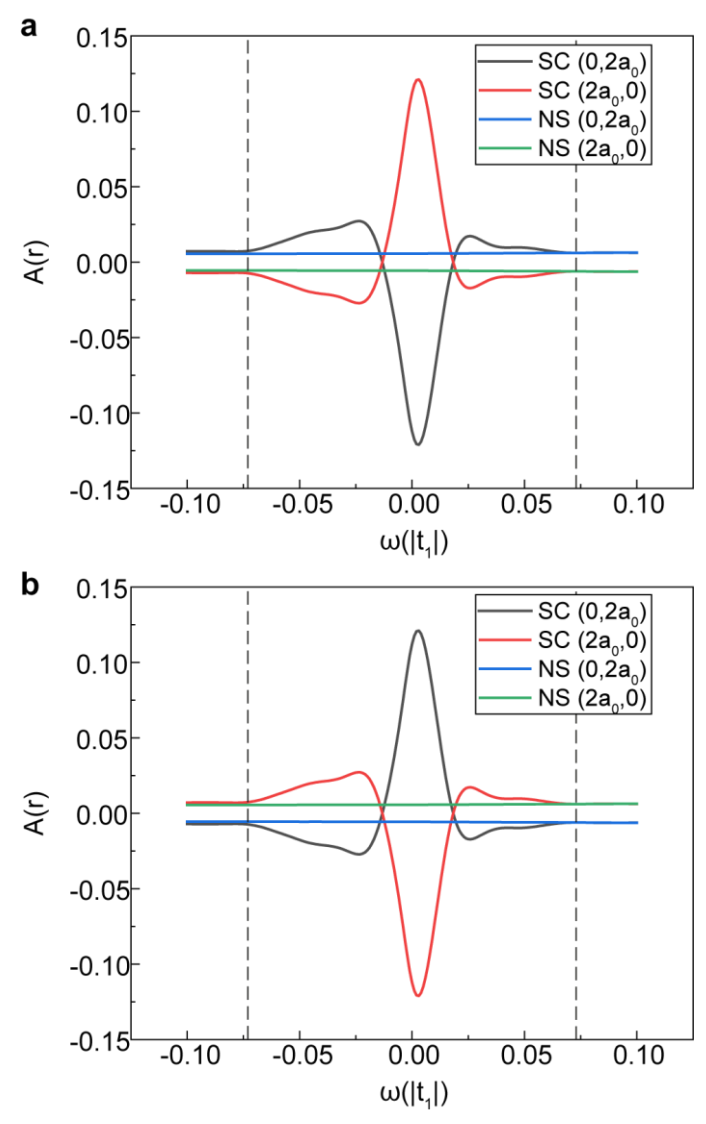


Figure S4. Local anisotropy as a function of energy along high symmetry directions (1,0) and (0,1) with the parameters described in section 1.

**a,b** Local anisotropy  $A(\mathbf{r}, E)$  at two sites away from the impurity along (1,0) (red curve) and (0,1) (black curve) with the impurity positioned at sublattice  $\mathbf{a}$  (a) and sublattice  $\mathbf{b}$  (b). Green (blue) curve is the local anisotropy  $A(\mathbf{r}, E)$  of the model in the normal state along (1,0) ((0,1)) obtained by setting  $\{\Delta_1, \Delta_2\} = \{0.0, 0.0\}$ . Black dashed lines indicate the energy of superconducting gap  $\Delta$ .

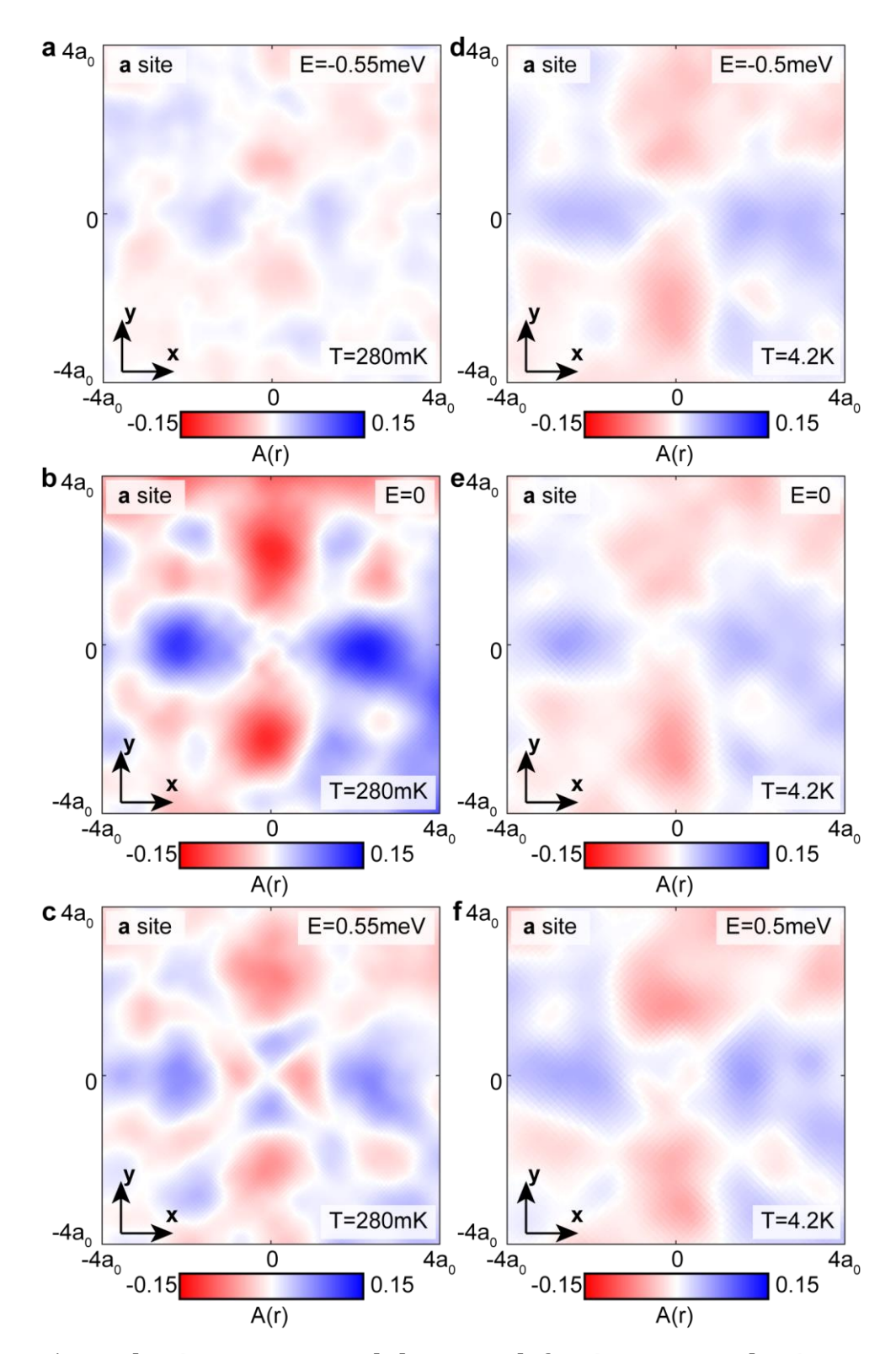
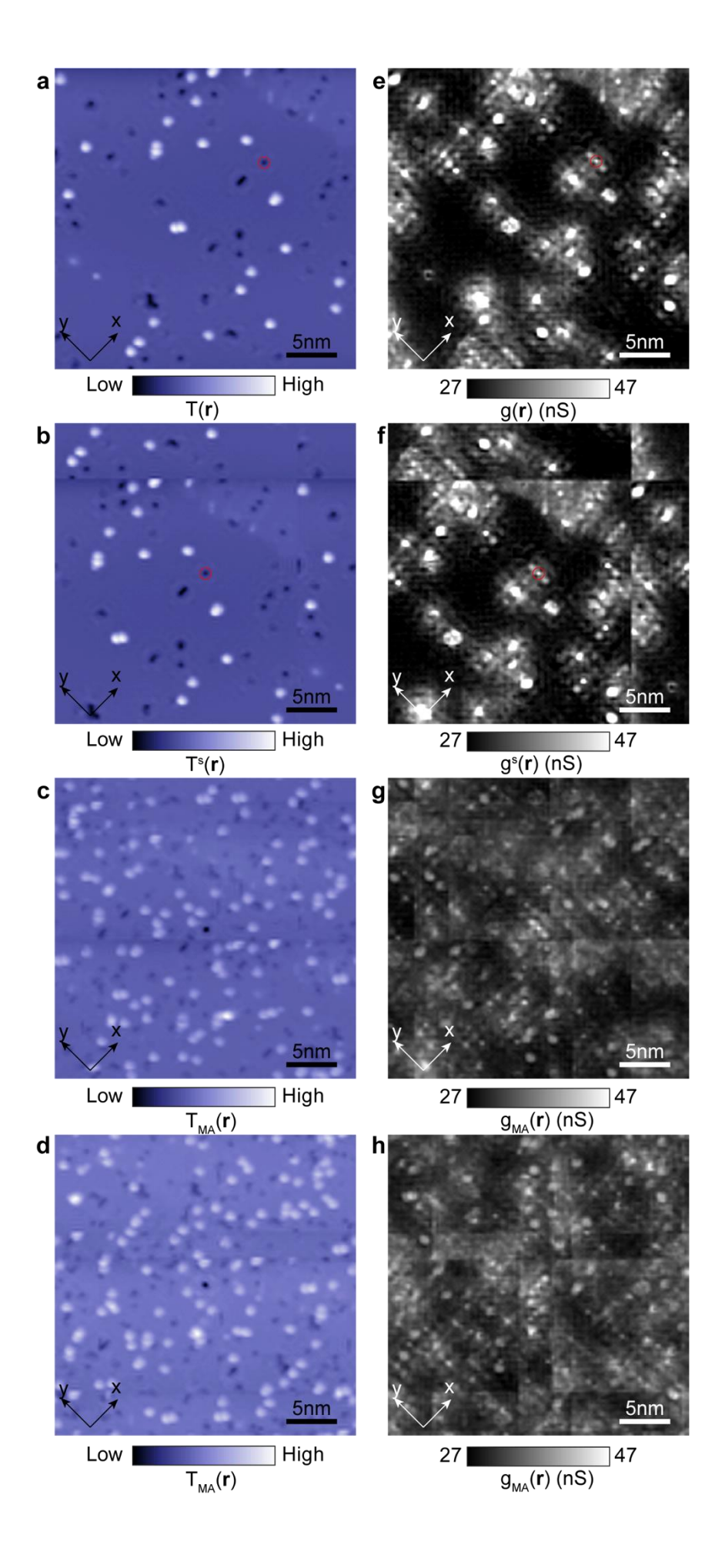


Figure S5. Local anisotropy around the same defect in superconducting state and in normal state

**a,b,c** Local anisotropy  $A(\mathbf{r}, E)$  around the defect at sublattice  $\mathbf{a}$  at E=-0.55 meV( $\mathbf{a}$ ), E=0( $\mathbf{b}$ ) and E=0.55meV( $\mathbf{c}$ ) at T=280mK well below the superconducting temperature  $T_c = 2.3K$ .

**d,e,f** Local anisotropy  $A(\mathbf{r}, E)$  around the same defect in **a,b,c** at E=-0.5 meV(**a**), E=0(**b**) and E=0.5meV(**c**) at T=4.2K well above the superconducting temperature  $T_c = 2.3K$ .



## Figure S6. Multi Atom Analysis of Experimental Data in large FOV

- **a,e** CeCoIn<sub>5</sub> topography (**a**) and  $g(\mathbf{r}, E = 0)(\mathbf{e})$  with a defect (shown by red circle) not at the center of the FOV.
- **b,f** Inverse Fourier transform after applying shift theorem (Eqn. S14,S15) to the Fourier transform of a(**b**) and e(**f**) with the defect position marked by the red circle. The defect is shifted to the center of the FOV with periodic boundary conditions.
- **c,g** The MA-averaged topography (c) and  $g(\mathbf{r}, E = 0)(\mathbf{g})$  of the defects at sublattice  $\mathbf{a}$
- **d,h** The MA-averaged topography (**d**) and  $g(\mathbf{r}, E = 0)(\mathbf{h})$  of the defects at sublattice **b**

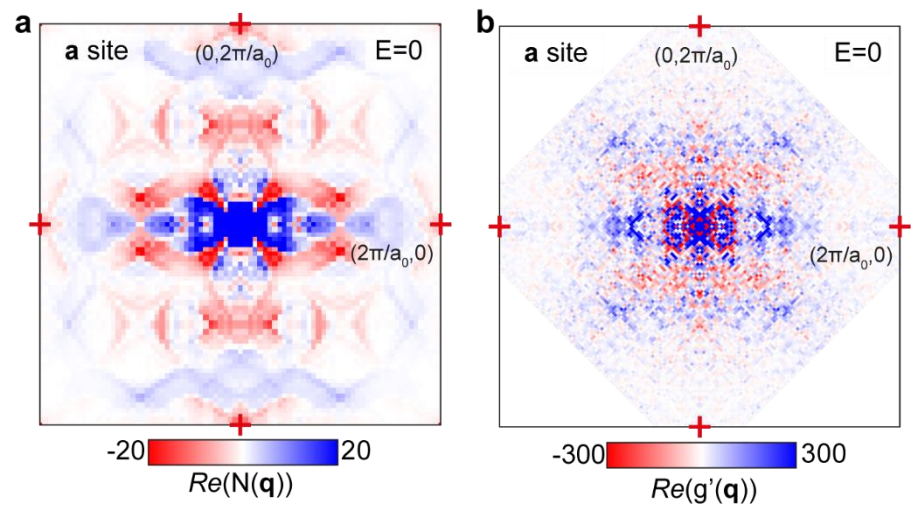


Figure S7. Fourier transformed BQPI N(q,E) at E=0

- **a** Fourier transformation of the theoretical BQPI pattern  $N(\mathbf{q}, E)$  with the impurity atom at sublattice  $\mathbf{a}$  at E=0. The  $\mathbf{r}$ -space center of the transformation is set at the impurity site.
- **b** Real parts of Fourier transformed MA-averaged differential conductance map  $Re(g'(\mathbf{q}, E))$  at  $E \sim 0$  around the defects at sublattice  $\mathbf{a}$ . Identical to Fig. 5e included here for comparison.

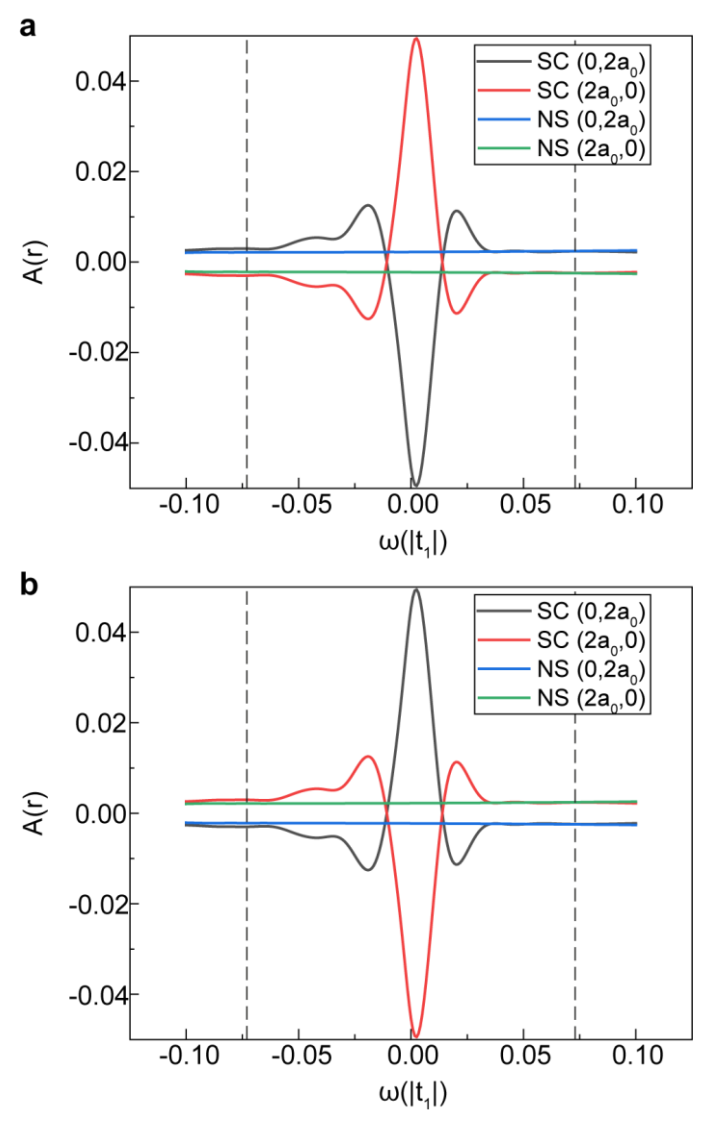


Figure S8. Local anisotropy as a function of energy along high symmetry directions (1,0) and (0,1) with  $\Delta_{oo}=0.1|t_1|$ 

**a,b** Local anisotropy  $A(\mathbf{r}, E)$  at two sites away from the impurity along (1,0) (red curve) and (0,1) (black curve) with the impurity positioned at sublattice  $\mathbf{a}$  (a) and sublattice  $\mathbf{b}$  (b). Green (blue) curve is the local anisotropy  $A(\mathbf{r}, E)$  of the model in the normal state along (1,0) ((0,1)) obtained by setting  $\{\Delta_1, \Delta_2\} = \{0.0, 0.0\}$ . Black dashed lines indicate the energy of superconducting gap  $\Delta$ .

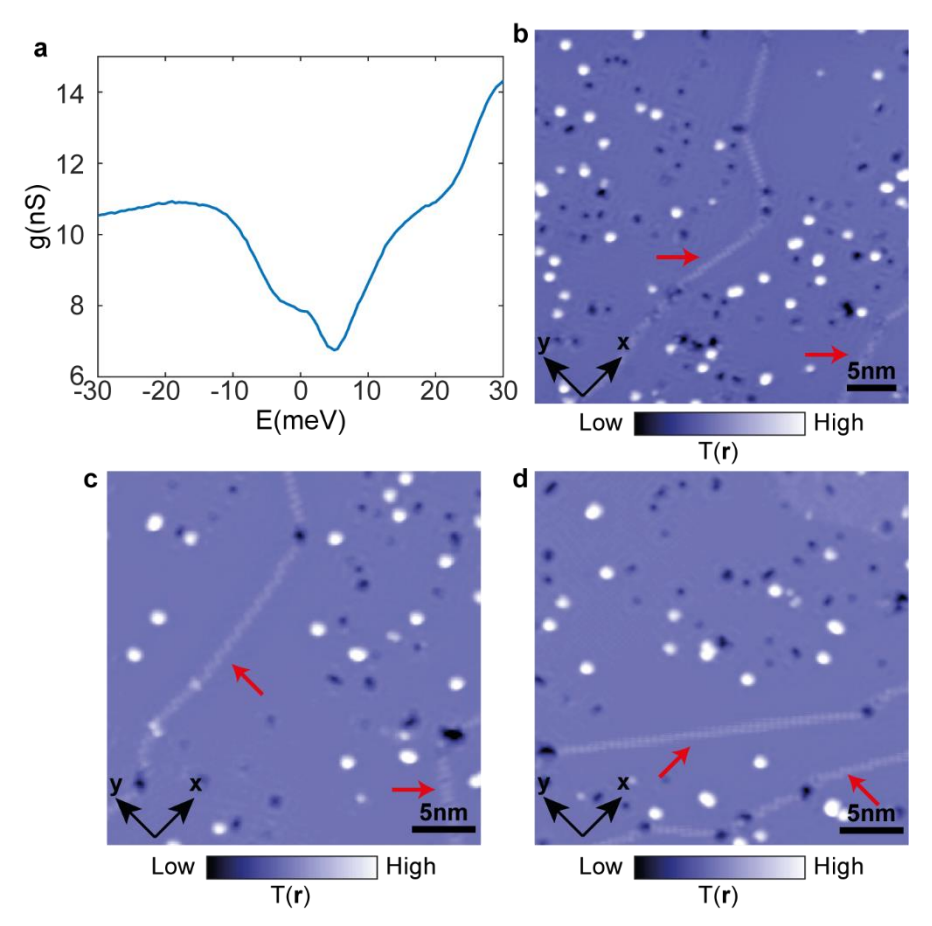


Figure S9. Determining cleaved surface

a Typical measured tunneling spectrum on cleaved surface.

**b,c,d** CeCoIn<sub>5</sub> topography with domain boundaries (marked by red arrows).

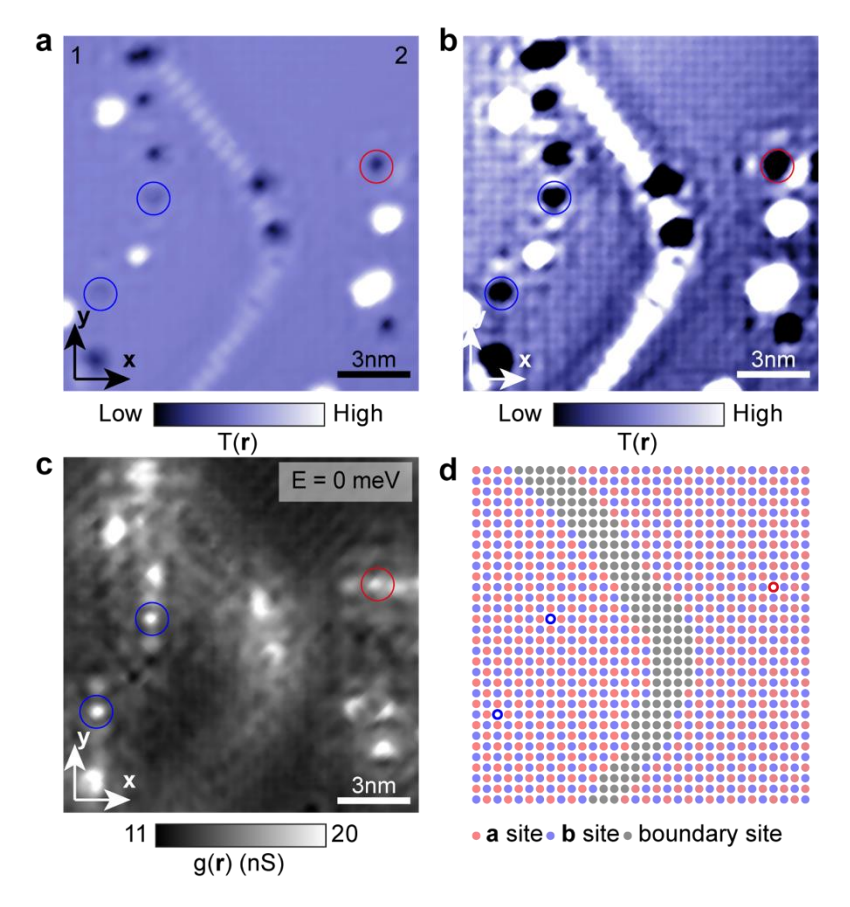


Figure S10. Orbital order domains near the domain boundary

- **a** CeCoIn<sub>5</sub> topography with two domains near a domain boundary.
- **b** The same topography in **a** with adjusted colormap limit to show the atom sites.
- **c** CeCoIn<sub>5</sub>  $g(\mathbf{r}, E = 0)$  in the same field of view in **a**.
- **d** The schematic diagram of the arrangement of atoms with orbital order marked by red dots (a site) and blue dots (b site), according to b,c. The atoms at the domain boundary are marked by gray dots. The hollow circles show the position of the defects, corresponding to the defects marked in a,b,c by blue (a site) or red circles (b site).

#### References:

1 Graser, S., Maier, T. A., Hirschfeld, P. J. & Scalapino, D. J. Near-degeneracy of several pairing channels in multiorbital models for the Fe pnictides. *New Journal of Physics* **11**, 025016, doi:10.1088/1367-2630/11/2/025016 (2009).

- 2 Choubey, P., Berlijn, T., Kreisel, A., Cao, C. & Hirschfeld, P. J. Visualization of atomic-scale phenomena in superconductors: Application to FeSe. *Physical Review B* **90**, 134520, doi:10.1103/PhysRevB.90.134520 (2014).
- 3 Kreisel, A. et al. Towards a quantitative description of tunneling conductance of superconductors: Application to LiFeAs. *Physical Review B* **94**, 224518, doi:10.1103/PhysRevB.94.224518 (2016).
- 4 Singh, U. R. *et al.* Evidence for orbital order and its relation to superconductivity in FeSe<sub>0.4</sub>Te<sub>0.6</sub>. *Sci Adv* **1**, e1500206, doi:10.1126/sciadv.1500206 (2015).
- 5 Sharma, R. et al. Multi-atom quasiparticle scattering interference for superconductor energy-gap symmetry determination. *Npj Quantum Materials* **6**, 7, doi:10.1038/s41535-020-00303-4 (2021).
- 6 Aynajian, P. et al. Visualizing heavy fermions emerging in a quantum critical Kondo lattice. *Nature* **486**, 201-206, doi:10.1038/nature11204 (2012).
- 7 Kim, H. et al. Atomic-scale visualization of surface-assisted orbital order. *Science Advances* **3**, eaao0362, doi:10.1126/sciadv.aao0362 (2017).